

# Lawrence Berkeley National Laboratory

## Lawrence Berkeley National Laboratory

**Title**

Ultrafast Magnetization Dynamics of SrRuO<sub>3</sub> Thin Films

**Permalink**

<https://escholarship.org/uc/item/6d16c6bt>

**Author**

Langner, Matthew C

**Publication Date**

2009-08-04

# Ultrafast Magnetization Dynamics of SrRuO<sub>3</sub> Thin Films

Matthew Clemens Langner  
Ph.D. Thesis

Department of Physics  
University of California, Berkeley

and

Materials Science Division  
Ernest Orlando Lawrence Berkeley National Laboratory  
Berkeley, CA 94720

Spring 2009

This work was supported under U.S. Department of Energy contract number  
DE-AC02-05CH11231.

**Ultrafast Magnetization Dynamics of SrRuO<sub>3</sub> Thin Films**

by

Matthew Clemens Langner

B.S. (University of California, Berkeley) 2001

A dissertation submitted in partial satisfaction of the  
requirements for the degree of  
Doctor of Philosophy

in

Physics

in the

GRADUATE DIVISION

of the

UNIVERSITY OF CALIFORNIA, BERKELEY

Committee in charge:

Professor Joseph Orenstein, Chair

Professor R. Ramesh

Professor Oscar Dubon

Spring 2009

# Ultrafast Magnetization Dynamics of SrRuO<sub>3</sub> Thin Films

Copyright 2009

by

Matthew Clemens Langner

The U.S. Department of Energy has the right to use this document for any purpose whatsoever including the right to reproduce all or any part thereof.

## Abstract

Ultrafast Magnetization Dynamics of SrRuO<sub>3</sub> Thin Films

by

Matthew Clemens Langner

Doctor of Philosophy in Physics

University of California, Berkeley

Professor Joseph Orenstein, Chair

Itinerant ferromagnet SrRuO<sub>3</sub> has drawn interest from physicists due to its unusual transport and magnetic properties as well as from engineers due to its low resistivity and good lattice-matching to other oxide materials. The exact electronic structure remains a mystery, as well as details of the interactions between magnetic and electron transport properties. This thesis describes the use of time-resolved magneto-optical Kerr spectroscopy to study the ferromagnetic resonance of SrRuO<sub>3</sub> thin films, where the ferromagnetic resonance is initiated by a sudden change in the easy axis direction in response to a pump pulse.

The rotation of the easy axis is induced by laser heating, taking advantage of a temperature-dependent easy axis direction in SrRuO<sub>3</sub> thin films. By measuring the change in temperature of the magnetic system in response to the laser pulse, we find that the specific heat is dominated by magnons up to unusually high temperature,  $\sim 100$  K, and thermal diffusion is limited by a boundary resistance between the film and the substrate that is not consistent with standard phonon reflection and scattering models.

We observe a high FMR frequency, 250 GHz, and large Gilbert damping parameter,  $\alpha \approx 1$ , consistent with strong spin-orbit coupling. We observe a time-dependent change in the easy axis direction on a ps time-scale, and we find that parameters associated with the change in easy axis, as well as the damping parameter, have a non-monotonic temperature dependence similar to that observed in anomalous Hall measurements.

---

Professor Joseph Orenstein  
Dissertation Committee Chair

For my family

# Contents

<b>List of Figures</b>	<b>iv</b>
<b>1 Introduction</b>	<b>1</b>
1.1 Spin-Orbit Interaction in SRO . . . . .	3
<b>2 SRO Thin Films</b>	<b>4</b>
2.1 Film Growth . . . . .	4
2.2 Electronic Properties . . . . .	6
2.2.1 Non-Fermi Liquid Behavior in SRO . . . . .	6
2.2.2 Anomalous Hall Effect . . . . .	7
2.3 Itinerant Ferromagnetism . . . . .	12
2.3.1 The Stoner Model . . . . .	12
2.4 Anisotropy . . . . .	13
2.4.1 Shape Anisotropy . . . . .	13
2.4.2 Magnetocrystalline Anisotropy . . . . .	14
2.5 Effect of Strain on Magnetic Properties . . . . .	15
2.6 Magnetic Anisotropy in SRO Thin Films . . . . .	15
<b>3 Magnetization Dynamics</b>	<b>17</b>
3.1 Damped Precession - Landau-Lifshitz-Gilbert Equation . . . . .	17
3.2 Magnetization Dynamics in Anisotropic Materials . . . . .	18
3.3 Spin Waves . . . . .	19
3.4 Damping . . . . .	20
3.4.1 Damping Due to Defects . . . . .	20
3.4.2 Direct Electron and Phonon Coupling . . . . .	20
3.4.3 Breathing Fermi Surface Model . . . . .	21
3.5 Measurements of Magnetization Dynamics . . . . .	22
3.5.1 Ferromagnetic Resonance . . . . .	22
3.5.2 Time-Resolved X-Ray Magnetic Circular Dichroism . . . . .	23
3.5.3 Time-Resolved Kerr and Faraday Effects . . . . .	23
<b>4 Ultrafast Magnetization Measurements</b>	<b>24</b>
4.1 The Magneto-Optical Kerr Effect . . . . .	24
4.1.1 Phenomenological Description . . . . .	24

4.1.2	Quantum Mechanical Description . . . . .	27
4.2	Magneto-Optical Kerr Measurements . . . . .	28
4.3	DC Kerr Measurements . . . . .	29
4.4	Time-resolved MOKE . . . . .	30
4.4.1	Optics . . . . .	30
4.4.2	Detection . . . . .	32
4.4.3	Derivative Measurements . . . . .	33
4.5	Cryostats . . . . .	34
4.6	Optical Bleaching Effects . . . . .	35
4.7	Exciting FMR in an Optical Experiment . . . . .	35
4.8	Laser Excitations of the Magnetic System . . . . .	36
4.8.1	Ultrafast Demagnetization . . . . .	36
4.9	Three Temperature Model . . . . .	37
4.10	Specific Heat Contributions in Metals . . . . .	38
4.10.1	Magnetic Specific Heat . . . . .	39
<b>5</b>	<b>Thermal Modeling of SRO Dynamics</b>	<b>42</b>
5.1	The Thermal Model and SRO . . . . .	42
5.1.1	Normalization of Laser Pulse Energy . . . . .	46
5.2	Heat Transfer Into the Substrate . . . . .	50
5.3	Finite-Difference Modeling . . . . .	53
<b>6</b>	<b>TR-MOKE on SRO - Magnetization Dynamics</b>	<b>55</b>
6.0.1	Critical Slowing Down . . . . .	55
6.1	Magnetic Precession - Fourier Analysis . . . . .	56
6.2	Components of Magnetic Response . . . . .	59
6.3	Modeling with linear response theory . . . . .	60
6.3.1	The Overshoot Model . . . . .	61
6.3.2	Longitudinal Changes in Magnetization . . . . .	62
6.4	Parameters of the Dynamics . . . . .	63
6.4.1	Link to the Anomalous Hall Effect . . . . .	64
6.5	Magnetic Dynamics and Sample Thickness . . . . .	66
6.6	Magnetic Dynamics of a Single Crystal . . . . .	67
6.7	SRO/Oxide Bilayers . . . . .	68
<b>7</b>	<b>Summary</b>	<b>70</b>
	<b>Bibliography</b>	<b>72</b>

# List of Figures

2.1	Lattice parameters of STO (left) and SRO (right) from 0 to 300 K. Figures adapted from [71] and [43]. . . . .	5
2.2	Left: Diagram of band shifting in the Stoner Model. Right: Calculated DOS for SRO [2] . . . . .	14
2.3	In-plane (red), out-of-plane (blue), and total magnetization (black) as a function of temperature. The angle of the easy axis relative to the sample normal is shown in the inset. Figure taken from [44]. . . . .	16
4.1	Schematic of energy levels in a ferromagnet. $\Delta_{ex}$ is the energy splitting from the exchange interaction, and $\Delta_{SO}$ is the spin-orbit splitting. Figure from [11]	28
4.2	Diagram of PEM output polarization with a retardation of $\frac{\lambda}{2}$ . The primary axes of the PEM are at 45 degrees to the linearly polarized light. . . . .	29
4.3	Diagram of time-resolved pump-probe setup . . . . .	31
4.4	Diagram of balanced photodetection scheme . . . . .	33
4.5	Calculated internal energy using the tight-binding model density of states . . . . .	41
5.1	Change in Kerr rotation as a function of time delay following pulsed photoexcitation on a 200 nm SRO/STO film. Left Panel: Temperature range $5K < T < 80K$ . Right panel: Temperature range $100K < T < 150K$ . . . . .	43
5.2	Change in Kerr rotation at $t = 25$ ps as a function of temperature. Different line colors correspond to different pump fluences. The inset shows the Kerr angle as a function of temperature . . . . .	43
5.3	$1/(\Delta T)$ , where $\Delta T$ is the calculated change in temperature, plotted for difference pump fluences. The black lines are fits to $T^{3/2}$ . . . . .	44
5.4	Left panel: Calculated $T_F$ vs. pump pulse intensity for different values of the equilibrium sample temperature. Right panel: Data shifted to lie on a common curve. . . . .	45
5.5	Left panel: Log-Log plot of the calculated internal energy vs. temperature for a 200nm SRO sample. Low temperature data fits at $T^{5/2}$ temperature dependence. Right panel: Calculated internal energy for 10nm, 50nm, and 200nm thick samples, plotted vs. $k_B T^{5/2}$ . . . . .	47

5.6	(a) Semi-log plot of 500 ps TR-MOKE signals for samples of various thickness. (b) Log of short time ( $t < 25$ ps) TR-MOKE signal plotted against $t^{1/2}$ , indicating stretched exponential behavior. (c) Decay times plotted versus sample thickness. (d) Decay times versus temperature for 200 nm (black, left axis) and 50 nm (red, right axis) films. . . . .	50
6.1	Left Panel: Numerical derivatives of TR-MOKE time traces. Right Panel: Fourier transforms of derivatives. . . . .	57
6.2	Left panel: Change in Kerr rotation as a function of time delay following pulsed photoexcitation at $T=5$ K, for several values of applied magnetic field ranging up to 6 Tesla. Right panel: Fourier transforms of signals shown in left panel. Inset: FMR frequency vs. applied field. The fitted line is consistent with a g factor of 2. . . . .	58
6.3	Left panel: Magnitudes of Fourier peaks as a function of temperature. Right panel: FT line-shapes normalized by pump intensity for several values of pump intensity at 5 K. . . . .	60
6.4	Left panel: Fit to the overshoot model in the time domain. The black line represents the data at 40K, and the red line is the fit. The blue line is the difference between the two. The green line represents a plot of the LLG equation with appropriate frequency and damping, with the amplitude set by the magnitude of the data at $t = 20$ ps. Right panel: Fit and data in the frequency domain . . . . .	62
6.5	Temperature dependence of (a) FMR frequency (triangles) and damping parameter (circles), (b) overshoot decay time, (c) ratio of overshoot amplitude to step-response amplitude ( $\phi_1/\phi_0$ ), and (d) $\sigma_{xy}$ (adapted from [64]) . . . .	64
6.6	Left: Damping parameter as a function of sample thickness. Right: Fourier transforms of 5, 10, and 50 nm samples. . . . .	66
6.7	Left: TR-MOKE signal at $t = 25$ ps on SRO single crystal for different pump attenuations. Right: Representative TR-MOKE time-traces recorder with $ND = 1.04$ . . . . .	67
6.8	FT line shapes for a 50 nm SRO film (black), and a 50 nm SRO film with a 10 nm BFO overlayer (red). . . . .	68

## Acknowledgments

Many people helped contribute to the work that went into this thesis. My advisor Joe for all of his guidance, and Ramesh for being the motivating force for a lot of this work. My coworkers: Colleen who worked with me on a lot of the experiments in this thesis, Chris, Nuh, and Jake for their mentorship. Special thanks to Lane, Eddie, Pu, and Wolter, who grew all of the samples that I studied. The support staff at LBL: Rene, Frank, Evan. The support staff in the Physics department: Anne, Donna, and Claudia. Most importantly my friends and family for their support outside of the lab: Mom, Dad, Jenni, Pam, Abby. The Psi Stars, BLFC, and Meerkats FC.

# Chapter 1

## Introduction

Understanding and eventually manipulating the electron's spin degree of freedom is a major goal of contemporary condensed matter physics. As a means to this end, considerable attention is focused on the spin-orbit interaction, which provides a mechanism for control of spin polarization by applied currents or electric fields. Despite this attention, many aspects of spin-orbit coupling are not fully understood, particularly in itinerant ferromagnets where the same electrons are linked to both rapid current fluctuations and slow spin dynamics.

SrRuO<sub>3</sub> (SRO) is a material well known for its dual role as a highly correlated metal, and an itinerant ferromagnet with properties that reflect strong spin-orbit (SO) interaction. Ferromagnetic resonance (FMR) provides direct information about the SO coupling but is unobservable in a standard FMR experiment due to the high precession frequency induced by the SO coupling.

Over the past decade, ultrafast magnetization measurements have provided an experimental tool capable of measuring magnetization dynamics on the time-scales of fundamental spin relaxation and precession. SRO is an ideal system for this type of measurement. A temperature-dependent easy axis direction allows for near instantaneous perturbation of the magnetic equilibrium in response to the pump pulse, and due to the strong spin-orbit coupling, the resulting response occurs on time-scales too fast for other experimental methods.

Work on time-resolved magneto-optics on SRO thin films was done previously by Ogasawara et al. [70], as part of a larger survey of temperature-induced changes in magnetism in thin films. The data included temperatures down to 77K on a 600 nm SRO/STO thin film for a single pump fluence. This data was taken on a nanosecond time-

scale. This thesis is a more detailed look at the SRO system, encompassing a wider range of temperatures, sample thicknesses, and time-resolutions that allows for the observation of physics not observable within the parameters of the previous study.

The following paragraphs offer a brief outline of the structure of this thesis.

Chapter 2 provides an overview of the properties of SRO thin films, including discussion of the magnetic properties and a brief discussion of the unusual electronic transport. The focus of this thesis is FMR, which is intimately linked to the magnetic anisotropy. SRO exhibits a low Curie temperature, indicating small spin-spin coupling, but strong coupling of spins to the magnetic easy axis. In thin films, both intrinsic and extrinsic anisotropies play a role in determining the easy axis direction. Electron transport is coupled to the magnetization through spin-scattering contributions to the resistivity and through the anomalous Hall effect.

Chapter 3 gives an outline of the theoretical constructs needed to model magnetization dynamics. Uniform magnetic precession and damping is treated phenomenologically through the Landau-Lifshitz-Gilbert equation while microscopic mechanisms leading to the damping are still unknown. While the full picture remains unclear, spin-orbit coupling plays a key role in many microscopic theories of damping. In addition to uniform magnetization precession, the thin film structure allows for coherent, non-uniform magnetization dynamics that exist in the form of standing spin-waves that can contribute to the time-resolved signal.

Chapter 4 details the experimental setup of the ultrafast magnetization measurements, and describes the fundamentals behind optical magnetization measurements. The successful interpretation of the optical measurement depends on properly describing the flow of energy from the electrons excited by the laser to other forms of energy in the system. The three temperature model describes this energy flow in terms of electron, phonon, and spin temperature baths.

In Chapter 5 we present analysis of the thermal aspects of our optical measurements. After laser excitation, the magnetization quickly settles into a higher-temperature equilibrium state. By comparing the laser-induced magnetization change with the magnetization temperature dependence, we can determine the functional form of the specific heat. Time-resolved measurements also provide insight into the subsequent flow of heat out of the system, which we analyze within the three temperature model.

In Chapter 6, we discuss the characterization of the magnetization precession and anisotropy dynamics induced by the laser pulse. We find that a modification of the Landau-Lifshitz-Gilbert equation provides a good description of the dynamics, and that both the

magnetic damping and the time-dependence of the anisotropy direction suggest a link between the magnetization dynamics and previously observed electron transport effects.

## 1.1 Spin-Orbit Interaction in SRO

One property that makes SRO stand out from other materials is an exceptionally strong spin-orbit interaction. The spin-orbit interaction has implications for many material properties:

- (1) Magnetization dynamics, in that it sets the strength of the magnetic anisotropy and is an important factor in precessional damping
- (2) Heat transfer, in that it communicates relative temperatures between the spins and electrons
- (3) Electron transport, in that it plays an integral role in the anomalous Hall effect.

Because spin-orbit coupling is required for understanding such a wide range of topics, I'll give a brief description of it straight-away.

Spin-orbit coupling is a result of the relativistic motion of the electrons relative to the periodic potential of the lattice; the moving electrons see the stationary electric potential as an effective magnetic field. The spin orbit coupling can be written in terms of the electron momentum  $\mathbf{p}$  and potential  $V$  as:

$$H_{SO} = -\frac{1}{4m^2c^2}\hat{\sigma} \cdot (\mathbf{p} \times \nabla V). \quad (1.1)$$

Here,  $m$  is the electron mass,  $c$  the speed of light, and  $\hat{\sigma}$  a vector representing the electron spin. The most direct effect of the effective magnetic field is to create a preferred direction for the alignment of the electron spins. This creates a magnetic anisotropy, as discussed in section 2.4.2, which in SRO has previously been measured as having an effective field strength of several tesla [62]. Because spin-orbit coupling is a relativistic effect, this strong spin-orbit coupling has been attributed to the relatively high charge of the Ru atoms.

## Chapter 2

# SRO Thin Films

Single crystal SrRuO<sub>3</sub> (SRO) is an itinerant ferromagnet with a Curie temperature ( $T_C$ ) of 160K [58]. Although it is considered to be metallic, electron-electron correlations are thought to play a significant role in determining the transport properties. This chapter describes the basic physics relevant to the transport and magnetic behavior, and discusses the specific properties of SRO thin films.

### 2.1 Film Growth

SRO films grown on SrTiO<sub>3</sub> (STO) substrates are the focus of this thesis, although films grown on DyScO<sub>3</sub> and GdScO<sub>3</sub> were also studied. STO is the substrate of choice due to close lattice matching with SRO crystals and the ability to manipulate the growth of the SRO films through substrate miscuts. SRO single crystals have a pseudo-cubic perovskite structure with lattice parameters  $a = 5.53 \text{ \AA}$ ,  $b = 5.57 \text{ \AA}$ , and  $c = 7.84 \text{ \AA}$ [43]. Thin films grown on (001) STO substrates have lattice parameters  $a = 5.55 \text{ \AA}$ ,  $b = 5.56 \text{ \AA}$ , and  $c = 7.85 \text{ \AA}$ . Relative to single crystals, thin films have a reduced Curie temperature, from 160 K in single crystals to 150 K in thin films [29], and higher residual resistivities [15, 45].

The data in this thesis were taken on films grown by pulsed-laser deposition or molecular beam epitaxy. Pulsed-laser growth was done at 680-700°C in 100 mTorr oxygen, and high-pressure reflection high-energy electron diffraction (RHEED) was used to monitor the growth of the SRO film in-situ. By monitoring RHEED oscillations, SRO growth was determined to proceed initially in a layer-by-layer mode before transitioning to a step-flow mode. RHEED patterns and atomic force microscopy imaging confirmed the presence of surfaces consisting of atomically flat terraces separated by a single unit cell step (  $3.93 \text{ \AA}$ ).

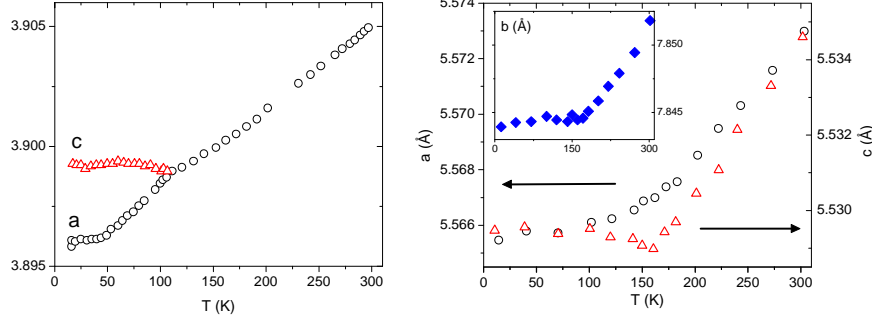


Figure 2.1: Lattice parameters of STO (left) and SRO (right) from 0 to 300 K. Figures adapted from [71] and [43].

X-ray diffraction indicated fully epitaxial films and x-ray reflectometry was used to verify film thickness.

STO substrates provide a good lattice match for SRO films, and by using a substrate with a miscut growth plane, structurally mono-domained samples can be grown [36]. On (001) oriented STO substrates, SRO films can grow with either the (001), (110), or  $(1\bar{1}0)$  plane oriented parallel to the STO surface. The STO substrate has a cubic crystal structure, and for a non-miscut, (001) oriented substrate, the (010) and (100) directions are indistinguishable. The miscut introduces a slight slant to the substrate plane that breaks the symmetry between two orthogonal in-plane directions. This creates a preferential growth direction for the SRO film, which can be achieved with a miscut of less than  $1^\circ$ . The SRO grows with the b-axis perpendicular to the sample plane, with the a-axis lying along the direction of the miscut.

In general, the lattice parameters of the substrate and film are temperature dependent, which leads to a temperature dependent strain in the thin film through thermal expansion mismatch.  $\text{SrRuO}_3$  exhibits the Invar effect; the lattice parameters are nearly constant as a function of temperature, with small fractional changes,  $\frac{\Delta a}{a} \approx 10^{-4}$ , over a temperature range from 0 to 300 K [43]. The temperature dependence of the lattice parameters show a change in slope at the magnetic transition temperature, with the temperature dependence becoming weaker in the magnetic phase. The magnitude of the change in the lattice parameters of  $\text{SrTiO}_3$  is similar to that of SRO, with a change in slope of the c-axis temperature dependence at a structural phase transition at 105 K [71]. This structural phase transition has no apparent effect on the properties of the SRO films.

## 2.2 Electronic Properties

Electron transport in SRO is complicated and often defies conventional theories. SRO is classified as metallic but exhibits lower conductivities than elemental metals such as Co and Fe by an order of magnitude. Hall effect measurements show the carrier concentration to be ( $2 \times 10^{22} \text{ cm}^{-3}$ ), lower than a typical metal but higher than high-temperature superconductors [45]. In addition, SRO shows evidence of strong electron correlations. In an attempt to summarize the electron transport properties, I'll start with brief description of Fermi Liquid Theory and continue with some highlights of relevant experimental results.

### 2.2.1 Non-Fermi Liquid Behavior in SRO

The simplest model for highly mobile electrons is that of a Fermi gas of non-interacting particles, and in many cases, this independent electron approximation gives an accurate picture of systems even with electron-electron interactions. While it would seem that the electron interactions would invalidate the independent electron approximation, the basis of Fermi Liquid Theory (FLT) is that interacting electrons can be treated as non-interacting electrons at low enough energy [61, 3].

The presence of electron-electron interactions renormalizes the energies for the single-particle wave functions, and these wave-functions are no longer stationary states of the system. FLT treats the system as a sum of single-particle wave-functions with renormalized energies (quasiparticles), with scattering between the single-particle states. If the scattering due to electron-electron interactions is slow relative to other scattering mechanisms, the single-particle approximation is valid. Often electron-electron induced scattering is relatively slow, due to a lack of available scattering states near the Fermi surface.

The failure of a systems to follow Fermi liquid-like behavior therefore indicates important electron-correlation effects, and can indicate novel electronic structure beyond the single-particle approximation [63]. An extreme case where the single-particle approximation breaks down is that of superconductivity, where the correct eigenstate is a Cooper pair of electrons. In SRO, the non-Fermi liquid (NFL) behavior has been modeled as originating from unusual hybridization between the ruthenium 4d electrons and oxygen 2p electrons [55].

The evidence for NFL behavior in SRO starts with the temperature dependence of the conductivity. At higher temperature, the resistivity of a normal metal saturates when

the mean free path becomes shorter than either the interatomic spacing or the de Broglie wavelength of the Fermi wave vector. This is known as the Ioffe-Regel limit. In SRO, the resistivity fails to saturate when the mean free path reaches the Ioffe-Regel limit around 500 K, indicating NFL behavior [2, 44, 23, 16]

Photoemission and IR conductivity studies provide further evidence that SRO behaves as a NFL [54, 28]. Photoemission spectra show a broader 4d Ru band than is expected from non-interacting band theory, and IR conductivity shows non-Fermi-like frequency dependence of the conductivity. For a Fermi liquid, the conductivity is expected to follow the Drude form, described by a representative scattering time  $\tau$  by [3]:

$$\sigma(\omega) = \frac{\sigma_0}{1 - i\omega\tau}. \quad (2.1)$$

The Drude conductivity follows a frequency dependence of  $\omega^{-2}$  at high frequencies. In SRO, the conductivity is shown to have a much weaker frequency dependence of  $\omega^{-1/2}$ , a result interpreted in the context of a frequency-dependent scattering rate  $\tau(\omega)$ .

The bad-metal properties of SRO are also thought to be responsible for spin-scattering effects on the resistivity observed below the Curie temperature [45]. The resistivity data show an unusually high divergence in the temperature derivative of the resistance ( $dR/dT$ ) at  $T_C$ , with different critical exponents for the divergences along different directions of the sample. The strong dependence of the resistivity on magnetic ordering is similar to other materials where band theory is inadequate to describe electron transport.

### 2.2.2 Anomalous Hall Effect

The aspect of electron transport most relevant to this thesis is the anomalous Hall effect (AHE). Anomalous hall conductivity is similar to the classic Hall conductivity, only instead of the off-diagonal term in the conductivity coming from an applied magnetic field, it is the result of the sample magnetization. The total Hall resistivity,  $\rho_{xy}$ , as function of temperature and magnetic field,  $H$ , is given by:

$$\rho_{xy} = R_0(T)H + R_s(T)M(T, H). \quad (2.2)$$

$R_0$  is the normal Hall coefficient, and  $R_s$  is the anomalous hall coefficient. The AHE is driven by spin-orbit coupling, which is necessary to couple the magnetization to the electron current [74, 85]. The AHE in SRO has a non-monotonic temperature dependence, and the origin of this behavior has been a matter of debate [64, 48, 27].

The debate centers on whether the AHE conductivity is driven by asymmetric scattering off of impurities or by intrinsic effects due to band structure. Experimentally the different contributions can be difficult to distinguish. The resistivity dependence of the AHE can distinguish between different extrinsic contributions but not between intrinsic and extrinsic contributions. Intrinsic and extrinsic effects may be distinguishable by the zero-temperature limit of the AHE, but a consensus is yet to form [8, 74, 68].

### Extrinsic Contributions to the AHE

The extrinsic scattering is impurity based and encompasses a classical asymmetric scattering mechanism known as skew-scattering [87] and a quantum mechanical scattering mechanism known as side-jump scattering [7]. Skew-scattering describes a situation where an electron traveling along a direction  $\phi = 0$  is scattered into a direction  $\phi = \phi'$  by a magnetic scattering center. The time-reversal symmetry breaking induced by the magnetic moment allows  $\phi'$  to be preferentially positive or negative, resulting in a net transverse flow of current. The side-jump mechanism also relies on this symmetry breaking, but instead of a change in propagation angle at the scattering center, the electron wave-packet undergoes an effectively instantaneous change in position transverse to its direction travel - i.e. an electron traveling in the  $+x$  direction jumps an amount  $\Delta y$ . This side-jump mechanism is a result of distortion of the electron wave-packet at the scattering center. In general, these two impurity effects will both contribute to the anomalous Hall conductivity, and for a simple single-spin model, they can be distinguished by the resistivity dependence of  $\rho_{xy}$ . For skew-scattering,  $\rho_{xy} \propto \rho_{xx}$ , while for the side-jump scattering,  $\rho_{xy} \propto \rho_{xx}^2$ .

### Intrinsic Contributions to the AHE

The theory of an intrinsic contribution centers on an anomalous velocity that occurs as the result of band structure. This theory was initiated by Karplus and Luttinger in 1954[59]. Karplus and Luttinger considered the perturbation of an applied electric field,  $H_E = e\mathbf{E} \cdot \mathbf{r}$  on electron Bloch wavefunctions altered by the spin-orbit interaction (equation (1.1)). Because of the modification of the Bloch wavefunctions, matrix elements of different bands become non-zero:

$$\langle u_{n',\mathbf{k}} | e\mathbf{E} \cdot \mathbf{r} | u_{n,\mathbf{k}} \rangle = ie\mathbf{E} \cdot \left\langle u_{n',\mathbf{k}} \left| \frac{du_{n,\mathbf{k}}}{d\mathbf{k}} \right. \right\rangle \neq 0, \quad (2.3)$$

where  $u_{n,\mathbf{k}}$  represents the periodic part of the Bloch function, and the bands are labeled by  $n$  and  $n'$ . These non-zero matrix elements lead to an anomalous transverse velocity.

Decades later, this was recognized as an effect of Berry's phase [74, 72, 27, 68]; the brief discussion of Berry's phase here is based on the review by Ong in reference [72]. Berry's phase is an additional phase that is picked up when a parameter,  $\mathbf{Q}$ , is integrated over a closed-loop in curved space, with the electron constrained to remain in the eigenstate specified by  $\mathbf{Q}$ . The phase,  $\chi$ , is dependent on the integral path  $C$ , and is written in terms of a vector potential,  $\mathbf{A}$ :

$$\chi(C) = - \oint_C d\mathbf{Q} \cdot \mathbf{A} \quad (2.4)$$

$$\mathbf{A} = \langle n, \mathbf{Q} | i \nabla_{\mathbf{Q}} | n, \mathbf{Q} \rangle. \quad (2.5)$$

The constraint in the Karplus-Luttinger anomalous velocity calculation is that the electron remain in the same energy band when the electric field is applied, and the integral path is the result of electron motion in  $\mathbf{k}$ -space due to the applied field. The resulting Berry's vector potential is:

$$\mathbf{X}(\mathbf{k}) = \int d^3r u_{n\mathbf{k}}^*(\mathbf{r}) i \nabla_{\mathbf{k}} u_{n\mathbf{k}}(\mathbf{r}), \quad (2.6)$$

where the integral is taken over the unit cell. This vector potential implies that the different indices of the position vector  $\mathbf{x}$  no longer commute, and the electron velocity is given by:

$$\hbar \mathbf{v} = -i [\mathbf{x}, H] = \nabla_{\mathbf{k}} \epsilon_n(\mathbf{k}) + \mathbf{E} \times \nabla_{\mathbf{k}} \times \mathbf{X}(\mathbf{k}). \quad (2.7)$$

The second term is the anomalous velocity from the Berry's phase, and the first term is the normal group velocity from the curvature of the energy band  $\epsilon_n(\mathbf{k})$ . The anomalous velocity has the desirable property of only appearing when the system breaks time-reversal symmetry, but it has the undesirable property of producing a resistivity dependence of the AHE indistinguishable from that of the side-jump mechanism,  $\rho_{xy} \propto \rho_{xx}^2$ .

Without a clear method to experimentally separate intrinsic from extrinsic effects, recent theoretical efforts have focused on comparing the relative sizes of the various contributions to the AHE. A calculation by Fang et. al showed that the intrinsic AHE is dominated by points in the band structure where the Fermi level is near degeneracies broken by the spin-orbit coupling [27]. A subsequent calculation of the size of this effect relative to the size of extrinsic effects suggested that in a regime of parameters satisfied by SRO, the intrinsic effect should dominate [75]. Linear response theory leading to the Kubo formula, described in the following section, was the the basis of the calculations the

intrinsic contribution to the AHE [27, 74]. The application of linear response theory is not limited to calculation of electron currents, and Onoda et al. postulated if the AHE is in fact dominated by near degeneracy points in the band structure, other physical observables should be as well [73].

### Kubo Formalism

Linear response functions describe the the response of a system to an external stimulus. Kubo formulas are linear-order calculations of these response functions from quantum-mechanical principles [56, 61]. The external force is treated as a perturbation to the equilibrium Hamiltonian, and the expectation value of the perturbing Hamiltonian is calculated while considering the time-evolution of the eigenstates.

To linear order, the eigenstates of the unperturbed system respond to the perturbation as:

$$|\phi(t)\rangle = |\phi_0\rangle - i \int_{-\infty}^t dt' H_1(t') |\phi(t)\rangle \quad (2.8)$$

$$\cong |\phi_0\rangle - i \int_{-\infty}^t dt' H_1(t') |\phi_0\rangle. \quad (2.9)$$

The second equation derives from the first by iteratively substituting the the expression for  $\phi(t)$  into the integral, and eliminating terms above linear order.

The response function of the system is calculated by using the time-dependent expression for  $\phi$  to calculate the change in expectation value for some system observable. We've assumed that the eigenstates of the system evolve smoothly under the perturbation, which is equivalent to assuming that the perturbation is turned on adiabatically. In the math, this is represented by introducing a parameter  $\eta$ , that represents the switch-on time of the perturbation. The results are considered in the limit  $\eta \rightarrow 0$ . The time-dependence of the observable under the perturbation is:

$$\langle x \rangle = \langle \phi(t) | x | \phi(t) \rangle \quad (2.10)$$

$$\cong \langle \phi_0 | x | \phi_0 \rangle - i \int_{-\infty}^t dt' e^{\eta t'} \langle \phi_0 | [x, H_1] | \phi_0 \rangle. \quad (2.11)$$

And the change in observable is then:

$$\delta \langle x \rangle = \langle \phi(t) | x | \phi(t) \rangle - \langle \phi_0 | x | \phi_0 \rangle \quad (2.12)$$

$$\cong -i \int_{-\infty}^t dt' e^{i\eta t'} \langle \phi_0 | [x, H_1] | \phi_0 \rangle. \quad (2.13)$$

In particular, the Kubo-Greenwood formula is a calculation of the frequency dependent conductivity, where the perturbation is treated as a vector potential:

$$A = \frac{cE}{i\omega} e^{-i\omega t} + \left( \frac{cE}{i\omega} e^{-i\omega t} \right)^*. \quad (2.14)$$

The conductivity relates the applied electric field,  $E$  to the expectation value of the current operator,

$$j = -\frac{e}{m} \left[ P + \frac{e}{c} A \right]. \quad (2.15)$$

The calculation is additionally complicated by the change in the momentum due to the vector potential,  $P \rightarrow P + \frac{e}{c} A$ . Combining all of these factors, the result is [74]:

$$\begin{aligned} \sigma_{xy}(\omega) &= \frac{\langle j_y \rangle}{E_x e^{-i\omega t}} = i \sum_{n \neq m} \sum_k \frac{f(\epsilon_m(k)) - f(\epsilon_n(k))}{\epsilon_n(k) - \epsilon_m(k)} \\ &\quad \times \frac{\langle nk | j_y | mk \rangle}{\omega - i\eta + \epsilon_m(k) - \epsilon_n(k)}. \end{aligned} \quad (2.16)$$

The bands are labeled by the indices  $n$  and  $m$ , with  $\epsilon_n$  representing the band energy. The functions  $f(\epsilon_n)$  represent the Fermi occupation factors at the band energies.

The Hall conductivity is the DC limit of the Kubo formula, and so we can make some loose generalizations about this function in reference to the discussion in section 2.2.2. Partial criteria for a dominant intrinsic AHE is the placement of the Fermi level near an avoided crossing in the band-structure. If the Fermi energy lies between two bands, the difference in the occupation functions will be relatively large:  $f(\epsilon_n) \gg f(\epsilon_m)$ . An avoided crossing implies that the energy difference between the two bands is small, meaning terms in the denominator of the form  $(\epsilon_m - \epsilon_n)$  will be small at the point in k-space corresponding to the avoided crossing relative to other terms in the sum over  $k$ . If the expectation value of  $j_y$  varies relatively smoothly in k-space, the sum in (2.16) will be strongly dependent on the terms representing the near degeneracy points.

## 2.3 Itinerant Ferromagnetism

Magnetic ordering is a result of Coulomb interactions that energetically favor the alignment of electron spins. Compared to electrons in a symmetric spatial state, electrons in an anti-symmetric spatial state have relatively lower Coulomb energy as they are relatively delocalized. This delocalization leads to a lower electrostatic energy from electron-electron interactions. The Pauli principle states that the overall electron state must be anti-symmetric, and the lowest-energy spin state is therefore symmetric [88]. The decrease in Coulomb energy for electrons in the anti-symmetric state therefore favors magnetic ordering. While discussions of the exchange interaction generally occur in the context of a prototype two-electron atomic model, the basic principle remains the same for more complicated structures, even while the calculations become much more complex.

In itinerant systems, the electrons carrying the ordered spins are highly mobile, and the magnetic ordering implies an energy difference between spin up and down electrons. The delocalized spins are exemplified by non-integer spin moments per atom [86]. Magnetism in SRO comes from electrons of 4d character from the Ru atoms, with the exchange mediated through hybridization with O 2p orbitals, and exhibit a zero-temperature saturated moment of  $\sim 1.6\mu_B/\text{Ru}$  [44, 15, 55].

### 2.3.1 The Stoner Model

The explanation of partial spin magnetic moments comes from band theory. The Stoner model is the simplest band model for itinerant magnetism, and describes itinerant ferromagnetism as a splitting in the bands for minority and majority spins resulting from the exchange interaction (the discussion in this section is based on information combined from references [61, 88, 56]). The shift of one band relative to the other places more states of the majority spin below the Fermi energy, and therefore there are more majority than minority spins. The net magnetization in this theory is then simply  $\mu_B(N_\uparrow - N_\downarrow)$ , where we've arbitrarily assigned the up spin to be the majority spin, and  $\mu_B$  is the Bohr magneton representing the magnetic moment of a single spin. A simple diagram illustrating the band splitting is shown in the left panel of figure 2.2. The right panel shows a calculation of the density of states for SRO done by Allen [2], with the majority band plotted on the top axis.

The band-splitting in the Stoner model comes at a cost of kinetic and potential energy, as the minority spins are effectively promoted to higher energies. Without the exchange interaction, the bands of the two spins are equal, and there will be a Fermi level,

$E'_F$ , with equal number of up and down spins occupied beneath it. The cost of favoring one spin over the other is the cost of taking one minority spin from beneath the energy  $E'_F$ , and placing it in the majority spin band above  $E'_F$ . This will be favored only if the band splitting lowers the Coulomb interaction energy (the exchange energy) more than this cost in kinetic energy. This is known as the Stoner criterion, and can be written as:

$$\frac{2\mu_B H_{mol}^0}{N_{\uparrow} + N_{\downarrow}} D(E_F) \geq 1, \quad (2.17)$$

where  $H_{mol}^0$  is the molecular field, and  $D(E_F)$  is the density of states at the Fermi energy.

The fundamental excitations in the Stoner model are spin-flips of the majority spin. In the case where the Fermi energy lies in the middle of both the majority and minority band, as shown in figure 2.2, this energy will be small. It is also possible for the majority level to be completely occupied, and for the Fermi energy to be above the highest level of the majority spin. In this case, there is a gap between the highest occupied majority state and the lowest unoccupied minority state. This gap is known as the Stoner gap, and materials possessing such a gap are termed 'strong' ferromagnets, whereas materials without such a gap are 'weak' ferromagnets.

The strength of the Stoner theory is its ability to reasonably explain fractional spin saturated moments for itinerant ferromagnets, but its main weakness comes from its failure to accurately predict the temperature dependence of the magnetization. In the Stoner theory, the temperature dependence comes from Fermi occupation functions of the minority and majority states at the Fermi level. Predictions based on this model fail to accurately predict the temperature dependent behavior of the magnetization, especially near the Curie temperature [88, 83].

## 2.4 Anisotropy

### 2.4.1 Shape Anisotropy

In a magnetized material, each spin experiences the dipole field of every other spin [18]. These dipole fields cancel each other, except for the fields produced by the free poles at boundaries of the material. This dipole field points in the direction opposite to the magnetization, is referred to as the demagnetization field. Because the field is created by the poles at the boundaries, the demagnetization energy is dependent on the shape of the material. For thin films, in which the x- and y- dimensions are much larger than the z-dimension, the dipole energy is given by [37]:

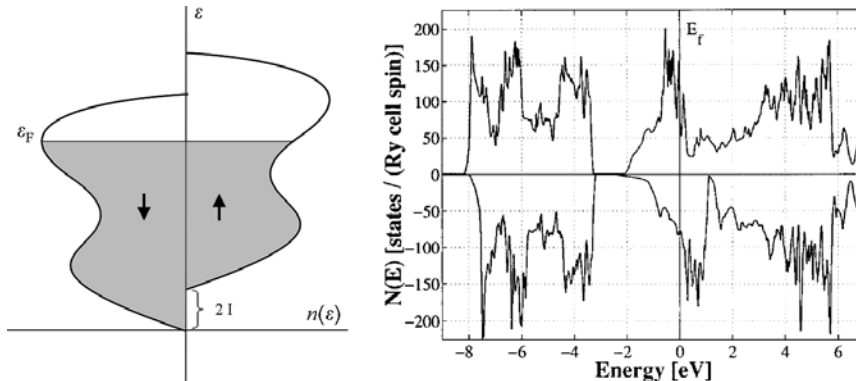


Figure 2.2: Left: Diagram of band shifting in the Stoner Model. Right: Calculated DOS for SRO [2]

$$E_d = \frac{1}{2}\mu_0 M^2 \cos^2\theta, \quad (2.18)$$

where  $\theta$  is the angle between the magnetization direction and the normal direction of the film. In thin-film geometry, the demagnetization energy favors alignment of the spins in the sample plane.

#### 2.4.2 Magnetocrystalline Anisotropy

In an anisotropic crystal, the internal energy is dependent on the direction of the magnetization. Intrinsic anisotropy is a result of spin-orbit coupling, where the spins choose a preferred direction due to the electronic structure [37]. The simplest case of anisotropy, and the type of anisotropy seen in SrRuO<sub>3</sub>, is uniaxial anisotropy, where alignment of the magnetization along a single direction is favored.

Energetically, uniaxial anisotropy is not the same as an applied magnetic field since in an anisotropic system alignment of the magnetization vector is favored either parallel or antiparallel to the anisotropy vector. Hence, the anisotropy energy can be written by expanding in even powers of an angle  $\phi$ , where  $\phi$  represents the deviation of the magnetization direction from the anisotropy direction [18]:

$$E_a = K_2 \sin^2(\phi) + K_4 \sin^4(\phi) + \dots \quad (2.19)$$

The signs of the coefficients  $K_i$  can be chosen such that the model system exhibits either uniaxial anisotropy ( $K_i > 0$ ) or easy-plane anisotropy ( $K_i < 0$ ).

## 2.5 Effect of Strain on Magnetic Properties

Additionally, the anisotropy of a thin film is affected by strain in what is essentially an inverse magnetostriction effect. The change of magnetization with applied strain is termed the Villari effect. Magnetostriction is a result of changing bond lengths in response to magnetization direction; the spin interaction energy is dependent both on the magnetization direction and distance between individual magnetic moments, and the ordered magnetization adds an additional dipole-energy term [18].

In a thin film without any external stresses applied, the internal strain is a result of the lattice mismatch between the film and the substrate [21]. The epitaxial layer is forced to match the lattice parameters of the substrate, causing a homogeneous strain across the interface and a distortion of the film normal to the surface. The distortions of the lattice parameters relax toward the bulk values in layers away from the substrate, leading to different strain effects in films of different thicknesses [76].

Calculations of SrRuO<sub>3</sub> structure suggest strong magneto-structural coupling, and therefore strong changes in magnetic properties under strain [99]. Magnetic measurements on SrRuO<sub>3</sub> indicate that strain reduces the saturated magnetic moment and lowers the transition temperature by about 10 K [29], even though the strain from lattice mismatch in SrRuO<sub>3</sub>/SrTiO<sub>3</sub> thin films is small - approximately 0.64%. The reduction in saturated moment indicates a reduction of the anisotropy due to the strain. The magnetic transition is also broader in temperature for thin films, indicating non-uniform strain through the sample.

The change in magnetic properties correlates with structural change in the oxygen octahedra, which can either tilt or deform in response to external strain. The high-spin state of SrRuO<sub>3</sub> is a result of four Ru electrons occupying three degenerate  $t_{2g}$  orbitals, leaving two spins uncompensated. A distortion of the bond lengths in the oxygen octahedron can lift the degeneracy of the  $t_{2g}$  orbitals, and a strong distortion can create a low-energy state where the Ru electrons occupy only two orbitals, with no net magnetic moment.

## 2.6 Magnetic Anisotropy in SRO Thin Films

SRO has an anisotropy field of several tesla (see section 1.1), and the direction of the easy-axis rotates in the a-b plane as the sample is cooled below the Curie temperature [44]. The easy axis makes an angle of approximately 45° to the film normal at the Curie temperature, and is aligned at approximately 30° from the normal as T approaches zero.

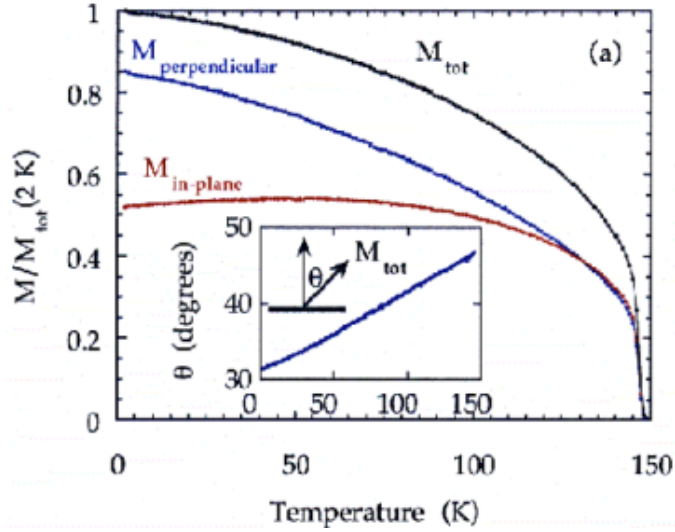


Figure 2.3: In-plane (red), out-of-plane (blue), and total magnetization (black) as a function of temperature. The angle of the easy axis relative to the sample normal is shown in the inset. Figure taken from [44].

The easy axis rotates further out of plane as the sample is cooled and the size of the magnetization increases, indicating that the easy axis rotation is due to changes in the intrinsic magnetocrystalline anisotropy and not due to shape anisotropy.

For a system with a rotating anisotropy direction such as SRO, the anisotropy is modelled with competing signs between the  $K_i$  coefficients in equation (2.19), i.e. a negative  $K_2$  and a positive  $K_4$ , where the magnitudes of  $K_2$  and  $K_4$  are temperature dependent. The equilibrium position for a system truncated at the  $K_4$  term is  $\sin(\phi_0) = \sqrt{-\frac{K_2}{2K_4}}$ .

The SRO/STO films are structurally monodomained, but can still be magnetically aligned either in or out of plane along the easy axis. The magnetocrystalline anisotropy terms in the free energy scale as even powers of  $|\mathbf{M}|$ , and the anisotropy energy is minimized for  $\mathbf{M} \parallel \mathbf{H}_A$  or  $(-\mathbf{M}) \parallel \mathbf{H}_A$ . In order to saturate the magnetization in the films during experiments, we cool the films in a magnetic field of  $\sim 0.5$  T. The divergence of the magnetic susceptibility at  $T_C$  allows us to align the magnetization with a moderate field when the sample is cooled through the transition. At low temperature, the coercive field needed to switch from one orientation to another, i.e.  $\mathbf{M} \rightarrow -\mathbf{M}$ , is less than 1 T.

## Chapter 3

# Magnetization Dynamics

### 3.1 Damped Precession - Landau-Lifshitz-Gilbert Equation

When a magnetic field is applied to a magnetic moment, the moment feels a torque that causes it to precess about the direction of the applied field. This precessional motion is the change in angular momentum due to the torque from the external field. The magnetic moment is related to the angular momentum through the gyromagnetic ratio,  $\gamma = -e\mu_0 g/2m_e$ . The equation of motion of a magnetic moment in an external field is then:

$$\gamma \frac{d\mathbf{L}}{dt} = \frac{d\mathbf{m}}{dt} = \gamma [\mathbf{m} \times \mathbf{H}]. \quad (3.1)$$

The torque experienced by a spin in a magnetic field originates from the commutation relations between spin operators [66]. The commutation relation is [73]:

$$[S_i, S_j] = i\hbar \epsilon_{ijk} S_k, \quad (3.2)$$

where  $\epsilon_{ijk}$  is positive one for right-handed permutations of x,y, and z, and negative for left-handed permutations.

These commutation relations come into the calculation of the time evolution of a quantum mechanical spin under an external magnetic field. The expectation value of the spin evolves according to the same quantum-mechanical rule for the time evolution of an operator [30]:

$$-i\hbar \frac{d\langle \mathbf{S} \rangle}{dt} = \langle [\mathbf{S}, H] \rangle. \quad (3.3)$$

Under an applied field,  $B$ , the appropriate Hamiltonian is:

$$H = -\frac{g\mu_B}{\hbar}\mathbf{S} \cdot \mathbf{B}. \quad (3.4)$$

Using the spin commutation relation (3.2), the calculation of (3.3) leads to:

$$\frac{d\langle\mathbf{S}\rangle}{dt} = \frac{g\mu_B}{\hbar}(\langle\mathbf{S}\rangle \times \mathbf{B}), \quad (3.5)$$

which is equivalent to (3.1).

The precessional motion will eventually decay and the magnetic moment will line up with the applied field. This behavior can be treated mathematically by adding a damping term to the equation for the precessional motion (3.1). Since the result of the damping is to decrease the amplitude of the precession, the damping torque is perpendicular to the direction of the magnetic moment. This phenomenological treatment of a damped precessional motion is described by the Landau-Lifshitz equation, where the damping is treated through a damping parameter  $\alpha$  [10, 88]:

$$\frac{d\mathbf{m}}{dt} = \gamma[\mathbf{m} \times \mathbf{H}] + \frac{\alpha\gamma}{|\mathbf{m}|}[\mathbf{m} \times (\mathbf{m} \times \mathbf{H})]. \quad (3.6)$$

The Landau-Lifshitz equation is appropriate for small damping parameters, but is not an accurate description when the damping is large. To better describe more highly-damped motion, a higher-order term in  $\alpha$  can be added to the Landau-Lifshitz equation, leading to the Landau-Lifshitz-Gilbert equation:

$$(1 + \alpha^2)\frac{d\mathbf{m}}{dt} = \gamma[\mathbf{m} \times \mathbf{H}] + \frac{\alpha\gamma}{|\mathbf{m}|}[\mathbf{m} \times (\mathbf{m} \times \mathbf{H})]. \quad (3.7)$$

This equation is commonly re-written as:

$$\frac{d\mathbf{m}}{dt} = \gamma[\mathbf{m} \times \mathbf{H}] + \frac{\alpha}{|\mathbf{m}|}\left[\mathbf{m} \times \frac{d\mathbf{m}}{dt}\right]. \quad (3.8)$$

## 3.2 Magnetization Dynamics in Anisotropic Materials

The magnetization dynamics in a uniaxially anisotropic material can be modeled using the LLG equation and an effective field due to the anisotropy. For the time-resolved magnetization dynamics in SRO, the motion is initiated through a sudden change in the anisotropy coefficients  $K_i$  from equation (2.19) in response to the laser pulse. To describe a shift in the equilibrium direction of the magnetization, such as that seen as a function of temperature in SrRuO<sub>3</sub>, at least two of the  $K_i$  must be non-zero. For small changes in the

equilibrium position, the potential well of an anisotropy characterize by  $K_2$  and  $K_4$  can be approximated by keeping only the lower order  $K_2$  term and considering the magnetization vector away from equilibrium at  $t = 0$ .

To fully describe the motion of the spins, the anisotropy, external magnetic fields, and the demagnetization field must be considered. Keeping only the lowest term in the anisotropy, and taking a coordinate system such that the magneto-crystalline anisotropy direction is along the z-axis, the full energy is given by [56]:

$$E = -\frac{1}{2}\kappa M_z^2 - \mathbf{H} \cdot \mathbf{M} + \frac{1}{2}(\mathbf{D} \cdot \mathbf{M})^2. \quad (3.9)$$

The vector  $\mathbf{D}$  points along the direction normal to the sample in the rotated coordinate system, and this term accounts for the shape anisotropy. The addition of anisotropy leads to an effective field given by:

$$\mathbf{H} = dE/d\mathbf{M}. \quad (3.10)$$

The inclusion of quadratic and higher order terms in the free energy to account for the anisotropy results in an effective magnetic field that is dependent on the direction of the magnetization vector, and hence the effect of the anisotropy in conjunction with an applied magnetic field is to produce an elliptical precession.

### 3.3 Spin Waves

Spinwaves are excitations of the uniform magnetization in the form of spin-flips spread over multiple spin sites. The thermal excitations of this type are discussed in chapter 4.10. Here, we're interested only in the effects of these spin waves on the magnetization dynamics.

In general these waves will travel through the sample in a manner determined by the spin-wave dispersion relation, but the geometry of thin films allows for the creation of standing spin waves (SSW) in the direction normal to the sample plane. These are spin waves with wave vector ( $\mathbf{q} = n\pi/L$ ) resonant with the sample thickness L. In the absence of any interfacial spin-pinning, the spins will be free to precess at the sample/substrate interface and at the sample surface, a configuration referred to as open boundary conditions.

The zero-order mode of the open-boundary SSW, known as the Kittel mode, is the uniform magnetization described by the LLG equation. A first-order SSW has been observed in optical dynamics measurements [93]. In this case, the sample thickness is longer than

the absorption depth of the exciting laser pulse, resulting in a non-uniform excitation of the sample that selectively excites this first-order mode.

## 3.4 Damping

In the LLG description of magnetization dynamics, damping of the magnetic motion is introduced phenomenologically. The damping represents a transfer of energy and momentum from the magnetic precession to other modes in the system. A complete description of the source of this damping will in general include many different scattering mechanisms, and the relative contributions from different sources is still the subject of study. A few theories of magnetic damping are described below. In metallic thin films, the predominant intrinsic damping mechanism stems from spin-orbit effects [33].

### 3.4.1 Damping Due to Defects

In addition to damping that occurs due to intrinsic material properties, extrinsic damping effects occur due to defects and other structural irregularities.

In a homogeneous system, spin-wave modes are decoupled and therefore do not exchange energy. Inhomogeneities in the magnetic system allow these modes to couple, allowing scattering between the uniform mode that represents the magnetic precession and higher order modes. This scattering mechanism does not transfer energy out of the magnetic system, but rather transfers energy between modes of the magnetic system [57].

Damping can also occur from irregularities in the direction of the anisotropy [4]. In this case, individual spins spiral into anisotropies that are not parallel to the anisotropy felt by the uniform precession. The stray spin is then pulled back into the precession by the exchange interaction, representing a transfer of energy away from the uniform precession. This process is known as 'dry magnetic friction', in reference to the fact that this type of damping occurs even if the precession is arbitrarily slow. Dry magnetic friction contributes to the damping only when the anisotropy is relatively strong in comparison to the exchange coupling.

### 3.4.2 Direct Electron and Phonon Coupling

A precessing magnetic moment can couple directly to electrons through Faraday's law; the changing magnetic field creates an electric field that induces a current in the

itinerant electrons. Energy is then lost from the magnetic precession through resistive losses in the current. For thin films, the damping parameter from this mechanism is [33]:

$$\alpha = \frac{M\gamma}{6} \left( \frac{4\pi}{c} \right) 2\sigma L^2. \quad (3.11)$$

Here  $M$  is the magnetization,  $\gamma$  the gyromagnetic ratio,  $L$  is the film thickness, and  $\sigma$  is the electrical conductivity. This type of damping can be identified relatively easily experimentally by either varying the sample thickness, or measuring the temperature dependence, which should be dominated by the temperature dependence of the electrical conductivity.

Magnetic precession couples to phonons through magnetoelastic deformations. As the magnetic moment precesses, shear waves are created in the film. This effect is appreciable only if resonant conditions exist for the elastic wave, and the resonant frequency is similar to that of the FMR frequency. Due to the long wave-length of such resonant modes, direct phonon coupling is not a significant contribution to precessional damping [49].

### 3.4.3 Breathing Fermi Surface Model

An early model explained the damping through scattering of itinerant s-p electrons with localized spins of d electrons. The damping results from a random torque created when itinerant s-p spins become mis-aligned relative to localized d-spins through scattering. The s-d model fails to give an accurate description of an itinerant ferromagnet system, as the electrons cannot be nicely divided into itinerant electrons and localized magnetic ones.

A theory without this limitation can be constructed by considering the spin-orbit Hamiltonian instead of the s-d exchange energy functional [40] [53]. Mathematically, the damping is calculated in a similar way as in the s-d model, using Kubo-Green formalism and the Random Phase Approximation [33]. The physical interpretation of the damping is based on the observation that the Fermi energy of a system with spin-orbit coupling is dependent on the magnetization direction. When a magnetic moment rotates and the Fermi energy changes, the electrons re-distribute in reaction to the change in Fermi surface. This redistribution occurs on a finite time scale, leading to a phase lag between the change in Fermi surface and electron redistribution that leads to magnetic damping. In the case of a precessing magnetization, the alteration of the Fermi surface is periodic, and therefore the model is referred to as the “breathing Fermi surface” model.

The breathing Fermi surface model gives a microscopic picture of the source of magnetic damping, but still treats the electron relaxation phenomenologically through the momentum relaxation time,  $\tau_m$ . The damping parameter is given by the relation [33]:

$$G \propto \int d\mathbf{k}^3 \sum_{\alpha, \beta, \sigma} \langle \beta | L^+ | \alpha \rangle \langle \alpha | L^- | \beta \rangle \delta(\epsilon_{\alpha, \beta, \sigma} - \epsilon_F) \hbar\omega \times \frac{\hbar/\tau_m}{(\hbar\omega + \epsilon_{\alpha, \mathbf{k}, \sigma} - \epsilon_{\beta, \mathbf{k}+\mathbf{q}, \sigma})^2 + (\hbar/\tau_m)^2}. \quad (3.12)$$

Here,  $\mathbf{q}$  represents a spin-wave momentum, and  $\sigma$  is the electron spin. The electron bands are represented by  $\alpha$  and  $\beta$ , and the damping parameter is proportional or inversely proportional to the relaxation time for intraband or interband scattering processes, respectively. The temperature dependence of the damping will scale with conductivity if intraband scattering is dominant, and with resistivity if interband scattering is dominant. As with the anomalous Hall effect, regions of k-space with near-degeneracies in the band structure can dominate the damping behavior from interband scattering [53].

### 3.5 Measurements of Magnetization Dynamics

There are several experimental methods to measure magnetization dynamics, a few of which are outlined below. All of the methods described below can be used to look at the uniform precession mode, and are therefore measurements of the magnetic anisotropy. Excluded are discussions of common methods such as Brillouin light scattering, which is used to measure the traveling spin-wave spectrum. A more complete list of magnetic characterization techniques can be found in references [26, 9]

#### 3.5.1 Ferromagnetic Resonance

In a ferromagnetic resonance (FMR) measurement, a DC magnetic field aligns the magnetization, and a small AC magnetic field perturbs the magnetization, causing a precession about the total effective field created by the sample anisotropy and the applied DC field,  $\mathbf{H}_{total} = \mathbf{H}_A + \mathbf{H}_{DC}$ . This process occurs in a microwave cavity, and microwave absorption is measured as the DC field is tuned. Tuning  $|\mathbf{H}_{total}|$  such that the precession frequency matches the microwave frequency enhances absorption of the microwave radiation. Hence, as the DC field is tuned, the peak absorption corresponds to the resonant frequency [32]. A typical FMR experiment can measure resonant frequencies up to  $\omega_0 \sim 70$  GHz.

The absorption of the microwave radiation is given by the imaginary part of the susceptibility and has a Lorentzian line-shape [33]:

$$\chi(\omega) \propto \frac{\Gamma}{(\omega - \omega_0)^2 + \Gamma^2}. \quad (3.13)$$

This function is peaked at  $\omega = \omega_0$ , where  $\omega_0$  is the resonant frequency of the magnetic precession. Information about the magnetic relaxation is given by the FMR line-width, represented by  $\Gamma$ .

### 3.5.2 Time-Resolved X-Ray Magnetic Circular Dichroism

X-Ray Magnetic Circular Dichroism (XMCD) exploits the difference in absorption between left and right circularly polarized x-rays in a magnetic material [79]. In basic principle this method is the same as the Kerr or Faraday effect, but with higher energy x-rays giving access to different quantum mechanical transitions. In the soft x-ray range, different atoms in complex materials have distinct absorption energies, and XMCD can distinguish between the magnetic contributions from these different atoms. Magnetic contrast between left and right circular polarizations is a result of dipole selection rules for different spin states.

Time-resolution of the XMCD signal is achieved with an experimental design similar to that of an optical pump-probe experiment. Polarized X-ray pulses act as the probe, and the system is pumped using short magnetic pulses from a coil. This requires synchronizing the x-ray pulses with the magnetic field pulses. In this way, magnetization dynamics for individual elements in a thin film can be studied. A time-resolved XMCD experiment has a time-resolution on the order of 1 ns.

### 3.5.3 Time-Resolved Kerr and Faraday Effects

Another optical technique utilizes ultrafast pulsed lasers and the effect of magnetization on the polarization of the laser pulses to measure fast magnetization dynamics. Ultrafast lasers typically generate pulses with pulse widths  $< 100$  fs, giving laser-based systems a time-resolution generally limited by the rise-time of the magnetic stimulus.

For SRO, this time-resolution is crucial to observing magnetization dynamics. The high magneto-crystalline anisotropy sets the resonance frequency ( $\nu_0$ ) above 200 GHz, beyond the frequencies measured by other techniques. Additionally, the magnetization can be perturbed by a laser-induced change in the magnetic anisotropy, making the switch-on time of the magnetic stimulus on the time-scale of the laser pulse. This technique will be discussed in greater detail in the following chapters.

## Chapter 4

# Ultrafast Magnetization Measurements

### 4.1 The Magneto-Optical Kerr Effect

#### 4.1.1 Phenomenological Description

The magneto-optical Kerr effect describes the change in the polarization of light when the light is reflected off of a magnetized material. For the case of transmitted light, the effect is referred to as the Faraday effect. The change in polarization is a result of time-reversal symmetry breaking, either through an applied magnetic field or spontaneous magnetic ordering. This time-reversal symmetry breaking can be described as a breaking of the symmetry between left and right handedness. Phenomenologically, the Kerr effect is a difference in index of refraction for right and left circular light caused by this intrinsic handedness.

The Kerr effect can be described by incorporating this symmetry argument into the formula for light propagation generated by Maxwell's equations. The symmetry breaking information is contained in the response function of the material. The displacement vector represents the response of a material to an external electric field, and is related to the field by a dielectric permeability tensor,  $\epsilon(\omega)$ :

$$\mathbf{D} = \epsilon_0 \epsilon(\omega) \mathbf{E}. \quad (4.1)$$

This dielectric tensor is incorporated into Maxwell's equations, which then describe the

propagation of an electric field in the material by:

$$\nabla \times (\nabla \times \mathbf{E}) = -\mu_0 \epsilon_0 \epsilon(\omega) \frac{\partial^2 \mathbf{E}}{\partial t^2}, \quad (4.2)$$

with plane-wave solutions of the form:

$$\mathbf{E} = \mathbf{E}_0 \exp[-i(\omega t - \mathbf{k} \cdot \mathbf{r})]. \quad (4.3)$$

The symmetry breaking from the magnetization dictates that the off-diagonal elements of the dielectric tensor are odd in the magnetization, and the diagonal elements even [84].

$$\epsilon_{ij}(\mathbf{M}, \omega) = \epsilon_{ji}(-\mathbf{M}, \omega). \quad (4.4)$$

The simplest case is that of a cubic material ( $\epsilon_{xx} = \epsilon_{yy} = \epsilon_{zz}$ ), where the only symmetry breaking comes from the magnetization. The dielectric tensor for a cubic material with an arbitrary magnetization can be written as [97, 98]:

$$\epsilon(\mathbf{M}, \omega) = \epsilon_{xx} \begin{pmatrix} 1 & -iQm_z & iQm_y \\ iQm_z & 1 & -iQm_x \\ -iQm_y & iQm_x & 1 \end{pmatrix}, \quad (4.5)$$

with

$$Q = i \frac{\epsilon_{xy}}{\epsilon_{xx}}. \quad (4.6)$$

The  $m_i$  represent the direction cosines of the magnetization  $\mathbf{M}$ . The off-diagonal terms proportional to  $\epsilon_{xy}$  are anti-symmetric with respect to time-reversal. The magnitude of the magnetization, and therefore the magnitude of the Kerr angle, is related to the magnitude of  $\epsilon_{xy}$ .

As equation (4.5) illustrates, the Kerr angle is dependent upon the relative direction of the light propagation to the magnetization direction. The simplest geometry, and therefore the most utilized experimentally, is the polar configuration, where the light propagation is along the direction of the magnetization, with both perpendicular to the material surface. As a result of the time-reversal breaking, the direction of the Kerr angle depends on whether the light propagation is parallel or anti-parallel to the magnetization, and is therefore non-reciprocal. In the longitudinal geometry, the magnetization is in both the sample plane and the plane of incidence of the light. The transverse geometry refers to the case where the magnetization is in the sample plane, but perpendicular to the plane of incidence.

For a magnetization in the z-direction, equation (4.5) simplifies to:

$$\epsilon(\mathbf{M}, \omega) = \begin{pmatrix} \epsilon_{xx} & \epsilon_{xy} & 0 \\ -\epsilon_{xy} & \epsilon_{xx} & 0 \\ 0 & 0 & \epsilon_{xx} \end{pmatrix}. \quad (4.7)$$

Considering the polar geometry, with  $\mathbf{k} \parallel \mathbf{M}$  and  $E_z = 0$ , and by using the dielectric tensor described in (4.7), equation (4.2) can be written in matrix form as:

$$\begin{pmatrix} \epsilon_0 \mu_0 \omega^2 - \epsilon_{xx} & -\epsilon_{xy} \\ \epsilon_{xy} & \epsilon_0 \mu_0 \omega^2 - \epsilon_{xx} \end{pmatrix} \begin{pmatrix} E_x \\ E_y \end{pmatrix} = 0, \quad (4.8)$$

which can be diagonalized as:

$$\begin{pmatrix} \epsilon_{xx} + i\epsilon_{xy} & 0 \\ 0 & \epsilon_{xx} - i\epsilon_{xy} \end{pmatrix} \begin{pmatrix} E_x + iE_y \\ E_x - iE_y \end{pmatrix} = 0. \quad (4.9)$$

The two eigenvectors correspond to right and left circularly polarized light, and the eigenvalues are the respective indices of refraction.

To consider the effect of the symmetry breaking on linearly polarized light, we can re-write the linearly polarized light as a linear combination of left and right circular polarizations:

$$\begin{pmatrix} 1 \\ 0 \end{pmatrix} = \frac{1}{2} \begin{pmatrix} 1 \\ i \end{pmatrix} + \frac{1}{2} \begin{pmatrix} 1 \\ -i \end{pmatrix} \quad (4.10)$$

$$\{linear\} = \{right\} + \{left\}.$$

The rotation of light of this polarization, which in general is complex, is given by

$$\theta_K = \frac{-2\epsilon_{xy}}{(\epsilon_{xx} + i\epsilon_{xy})(\epsilon_{xx} - i\epsilon_{xy}) - 1}. \quad (4.11)$$

Equation (4.11) is derived for a magnetization out of plane, with the laser along the magnetization. A full equation for the Kerr effect, including in-plane magnetizations and arbitrary angle of incidence, is derived in reference [97]. In terms of the components of the Fresnel matrix, the Kerr angles for light initially *s* or *p* polarized are:

$$\theta_K^p = \frac{r_{sp}}{r_{pp}} \quad (4.12)$$

$$\theta_K^s = \frac{r_{ps}}{r_{ss}}.$$

For initial medium with refractive index  $n_0$  and final medium with refractive index  $n_1$ , and for an angle  $\theta$  of the light away from normal, the Fresnel coefficients are given by:

$$\begin{aligned}
r_{pp} &= \frac{n_1 \cos \theta_0 - n_0 \cos \theta_1}{n_1 \cos \theta_0 + n_0 \cos \theta_1} - \frac{i2n_0 n_1 \cos \theta_0 \sin \theta_1 m_x Q}{n_1 \cos \theta_0 + n_0 \cos \theta_1} \\
r_{sp} &= \frac{in_0 n_1 (m_y \sin \theta_1 + m_z \cos \theta_1) Q}{(n_1 \cos \theta_0 + n_0 \cos \theta_1)(n_0 \cos \theta_0 + n_1 \cos \theta_1) \cos \theta_1} \\
r_{ps} &= -\frac{in_0 n_1 (m_y \sin \theta_1 - m_z \cos \theta_1) Q}{(n_1 \cos \theta_0 + n_0 \cos \theta_1)(n_0 \cos \theta_0 + n_1 \cos \theta_1) \cos \theta_1} \\
r_{ss} &= \frac{n_0 \cos \theta_0 - n_1 \cos \theta_1}{n_0 \cos \theta_0 + n_1 \cos \theta_1}.
\end{aligned} \tag{4.13}$$

#### 4.1.2 Quantum Mechanical Description

The off-diagonal component of the optical conductivity is calculated formally using the Kubo formalism [84], and the optical conductivity is directly related to the dielectric susceptibility discussed in the previous section through the formula:

$$\epsilon(\omega) = 1 + \frac{4\pi i \sigma(\omega)}{\omega}. \tag{4.14}$$

The equation for the off-diagonal optical conductivity calculated in the Kubo formalism is [61]:

$$\sigma_{xy} = -\frac{e^2}{im^2 \omega V} \left[ \sum_{nm} (f_n - f_m) \frac{\langle n | P_x | m \rangle \langle m | P_y | n \rangle}{E_n - E_m + \hbar\omega + i\eta} \right]. \tag{4.15}$$

In this equation,  $f_n$  is the occupation probability of state  $n$ ,  $P_{x,y}$  are momentum operators, and  $V$  is the total volume. Equation (4.15) is complex, with real and imaginary parts related by the Kramers-Kronig relations. The real part of equation (4.15) gives the absorption of incoming light, and the difference in absorption of right and left circular light gives a Kerr rotation. The dissipative part of the optical conductivity can be written in terms of right and left circular momentum operators ( $P_{\pm} = P_x \pm iP_y$ ) [11]:

$$\sigma''_{xy} = \frac{\pi e^2}{4\hbar\omega m^2 V} \sum_{nm} f_n [1 - f_m] \left[ |\langle n | P_- | m \rangle|^2 - |\langle n | P_+ | m \rangle|^2 \right] \delta(E_m - E_n - \hbar\omega). \tag{4.16}$$

Equation (4.16) shows that the difference in absorption between left and right circular light corresponds to a difference in transition rates between occupied states  $n$  and unoccupied states  $m$  for the different light polarizations. Quantum mechanically, the absorption of a photon is explained by electron dipole transitions between different energy bands. These transitions governed are by both momentum and energy conservation. The delta function

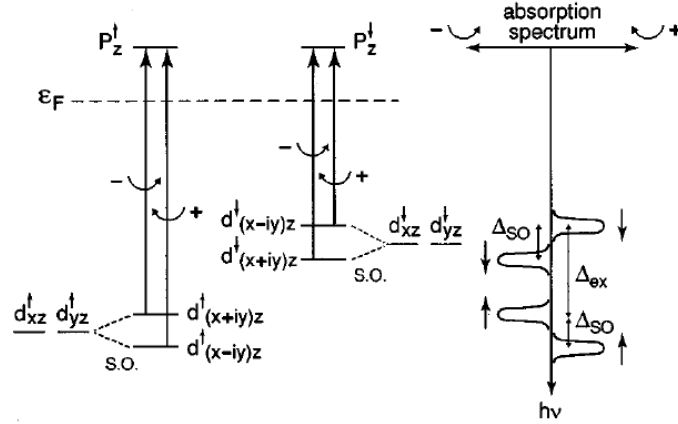


Figure 4.1: Schematic of energy levels in a ferromagnet.  $\Delta_{ex}$  is the energy splitting from the exchange interaction, and  $\Delta_{SO}$  is the spin-orbit splitting. Figure from [11]

in equation (4.16) accounts for energy conservation, and momentum conservation restricts the allowed transition states through the selection rules  $\Delta\ell = \pm 1$  and  $\Delta m_\ell = \pm 1$ .

The difference in absorption arises from the energy splitting caused by the exchange interaction and spin-orbit coupling. The exchange interaction splits energy levels with up and down spins, and spin-orbit coupling splits energy levels with different quantum numbers  $m_\ell$ . Right circular light selects a transition with  $\Delta m_\ell = 1$ , and left circular selects  $\Delta m_\ell = -1$ . An example for a  $d$  to  $p$  level transition is diagrammed in figure 4.1. Here, right and left circular polarizations cause transitions from  $m_\ell = \pm 1$  states to the same final state with  $m_\ell = 0$ .

## 4.2 Magneto-Optical Kerr Measurements

The goal of a magneto-optical Kerr measurement is to measure small changes in light polarization induced by a magnetized sample. Several schemes have been developed to measure such angles. Ultrasensitive measurements of the Kerr angle in SrRuO<sub>3</sub> thin films have been done as a function of temperature using an interferometry technique [46]. We utilize a simpler polarization modulation technique for DC characterization measurements, and a balanced photodetection scheme for time-resolved measurements. In both time-resolved and DC experiments, measurements were performed in the polar Kerr configuration.

For all measurements, we used a KM-Labs Ti:Saph laser to generate 100 fs laser pulses with a repetition rate of 90 MHz and center wavelength of 800 nm. Peak power

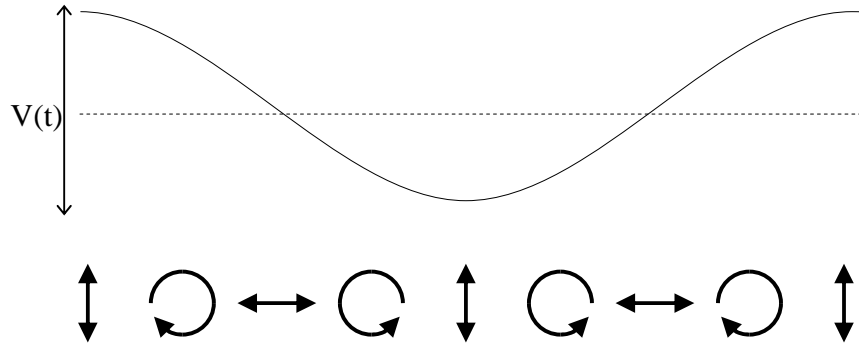


Figure 4.2: Diagram of PEM output polarization with a retardation of  $\frac{\lambda}{2}$ . The primary axes of the PEM are at 45 degrees to the linearly polarized light.

in pulse mode is approximately 500 mW at the laser output. The Ti:Saph laser itself is pumped with a diode-pumped Spectra-Physics Nirvana Nd:YVO<sub>4</sub> laser, with a wavelength of 532 nm and continuous 4.5 W output. The laser output has a slight divergence; so a lens pair is placed immediately outside the cavity to collimate the beam. To preserve the size of the beam waist, lenses of equal focal lengths are used. The back lens in the pair is mounted on a translation stage and its position finely adjusted to collimate the beam.

### 4.3 DC Kerr Measurements

For DC (non-time-resolved) measurements, we used a Hinds photoelastic modulator (PEM) to modulate the polarization of the light incident on the sample. The PEM is arranged such that the incoming light polarization is 45 degrees from the PEM's principle axes. The PEM causes a variable retardation of the light along one of the principle axes at a frequency of 50 kHz. A diagram of the light polarization coming out of the PEM is shown in figure 4.2. The intensity of the light reflected off of the sample is measured after passing through a polarizer aligned with the PEM's principle axes. Using this method, both the real and imaginary Kerr angles can be measured simultaneously. The imaginary Kerr angle, also called the ellipticity, is modulated at 50 kHz, while the real Kerr angle is modulated at 100 kHz.

For a given retardation  $A_0$ , the measured intensity is given by [69]:

$$I(t) = I_0 [1 + 2\theta_k J_0(A_0) - 4\epsilon_k J_1(A_0) \cos(\omega t) + 4\theta_k J_2(A_0) \cos(2\omega t)], \quad (4.17)$$

where  $J_n$  is the  $n^{\text{th}}$  Bessel function of the first kind. For retardation of 2.405 radians,  $J_0 = 0$ ,

and the Kerr angle can be recovered by dividing the signal at  $2\omega$  by the DC intensity:

$$\frac{I_{2\omega}}{I_{DC}} = \frac{4\theta_k J_2(A_0)}{\sqrt{2}(1 + 2\theta_k J_0(A_0))}. \quad (4.18)$$

The output of a single channel of a Nirvana balanced photodiode was connected to a lockin amplifier to make DC Kerr measurements. The lockin reads the signal modulated at 100 kHz, and the DC output of the Nirvana was averaged using one of the auxiliary inputs to the lockin. The lockin reads the RMS value of the modulated signal, leading to the factor of  $\sqrt{2}$  in the denominator of equation (4.18). The normalization of the  $2\omega$  signal must also be adjusted to account for the difference in gain between the balanced channel of the Nirvana at 100 kHz and the signal monitor at zero frequency. The difference in gain is a factor of 10, so the lockin reading at  $2\omega$  divided by the signal monitor gives  $(10 \times \theta_K)$  in radians.

## 4.4 Time-resolved MOKE

In a time-resolved pump-probe experiment, a pump pulse excites the sample, and the resulting changes to a much weaker probe pulse are measured to determine the effect of the excitation. Time resolution is achieved by varying the path length of the pump or probe pulse, which changes the relative arrival times of the two pulses. Beaurepaire et al. first utilized this pump-probe technique to measure magnetization dynamics in nickel thin films [5], where they observed a reduction in the magnetization on a picosecond time-scale in response to the pump pulse.

To make TR-MOKE measurements on SRO thin films, we utilize a reflection geometry. The SRO films have a penetration depth of approximately 37nm at a laser energy of 1.5 eV. Typical films were  $> 50$  nm thick, making them optically thick to the laser pulse. The sections below describe the optical setup for the time-resolved system, as well as the electronic scheme utilized to record the MOKE signal.

### 4.4.1 Optics

The time-resolution of the pump-probe system is ultimately limited by the temporal width of the laser pulse. The pulse width can be modified through alignment of the prisms in the laser cavity, but is also modified as the pulses travel through the optical system. As the laser pulse travels through the optics, the pulse width increases due to group velocity dispersion (GVD), as a result of the frequency-dependent refractive indices of the optics.

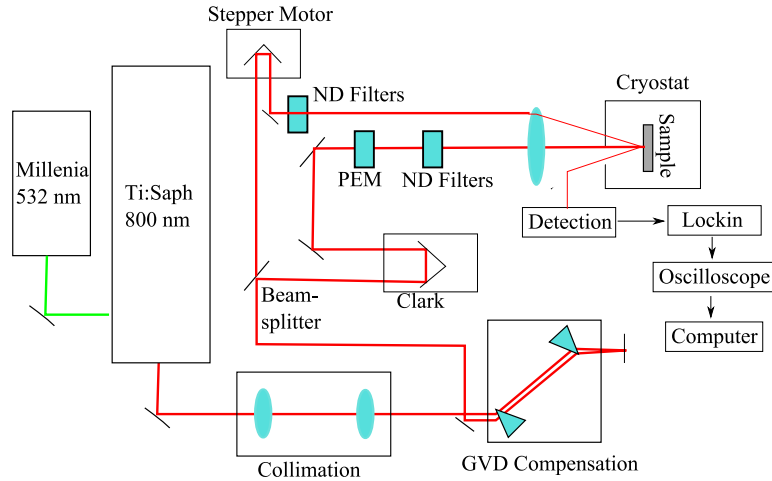


Figure 4.3: Diagram of time-resolved pump-probe setup

This pulse widening is pre-compensated using a prism pair. The refraction angle of the light through the prisms is frequency dependent, causing light of different frequencies to travel different path lengths going through the prism pair. This frequency-dependent path length induces a negative GVD in the laser pulse. To create a symmetric path through the prism pair, the prisms are rotated relative to the incoming beam to achieve minimum angular deviation of the beam.

A beamsplitter is used to separate the single beam into pump and probe paths. The beamsplitter reflects 90 percent of the laser power into the pump path, and the remaining transmitted power is used as the probe. Due to power loss through the optics, typical pump power at the sample is approximately 150 mW. Both pump and probe paths pass through neutral-density filters, with adjustable intensity from full power down to  $<1\%$  of full power.

The two beams are focused onto the sample using an achromatic doublet lens with a focal length of 150 mm. The spot size on the sample is approximately 100 microns, giving a maximum pump fluence of about  $0.1 \text{ J/cm}^2$  per pulse. We aligned the overlap between the two pulses by placing a 100 micron pin-hole in the laser path, and then adjusting the pin-hole position to maximize the reading on a power meter placed behind the pin-hole. The position of the pin-hole was adjusted to maximize the power of the pump beam, and then a steering mirror was used to maximize the probe beam power through the pin-hole.

To achieve time-resolution, the path length of either the pump or probe path can be altered, depending on the desired time-scale. To measure short delay times, we used a Clark fast-scanning delay line with a retroreflector in the pump path. The Clark continuously

varies the path length at a frequency of 22 Hz, with a time delay of approximately 50 ps. For long delay times, we use a retroreflector mounted on a Newport motorized translation stage in the probe path, which has a maximum delay of 500 ps. The 22 Hz repetitive scanning in Clark mode offers additional averaging over the stepper-motor data mode, and therefore gives a better signal-to-noise ratio. For the fast-scanning motion of the Clark to be stable, the retroreflector mounted on the Clark is small, with a diameter of approximately 1 cm. In order to achieve a clean reflection off of this retroreflector, the beam waste is reduced using a prism pair with a front prism with a focal length of 500 mm, and a back prism with a focal length of 100 mm.

#### 4.4.2 Detection

We measure the rotation of the probe beam by separating the light into horizontally and vertically polarized components with a Wollaston prism, and then measuring the intensity of the components using a Nirvana balanced photodiode. The balanced photodiode electronically subtracts photocurrent from two photodiodes, and therefore subtracts the intensities of the two perpendicularly polarized beams coming from the Wollaston. This subtraction makes the detection sensitive to rotations of the light's polarization, and also reduces noise from laser amplitude fluctuations. During measurements, we balance the DC signal of the Nirvana by rotating the polarization of the light before the polarizing beam-splitter, using a half-wave plate mounted in a Newport high-precision motorized rotation stage. Time-resolved ellipticity can be measured by balancing the Nirvana DC signal with a quarter wave-plate in place of the half wave-plate.

To record the changes in the polarization of the probe beam, we put the output from the Nirvana into a Stanford Research Systems SR850 lockin, which is referenced at the frequency of the modulation of the sample excitation. The sample excitation is modulated by chopping the pump beam at 100 kHz, which we achieve using the Hinds PEM. A polarizer is placed at the output of the PEM, and aligned perpendicular to the light polarization at the input (see figure 4.2). To normalize the size of the measured Kerr angle, the 100 kHz signal is divided by the DC signal from a single channel of the Nirvana, which is measured using one of the auxiliary inputs on the SR850. The gain settings on the lockin and differences in gain between the 100 kHz signal and DC signal on the Nirvana are corrected for in the data acquisition program. For measurements using the Newport stepper motor, the 100 kHz signal from the lockin is read directly to give the Kerr angle. All values read from the lockin are averaged at 512 Hz using the lockin's internal data register. To speed the transfer

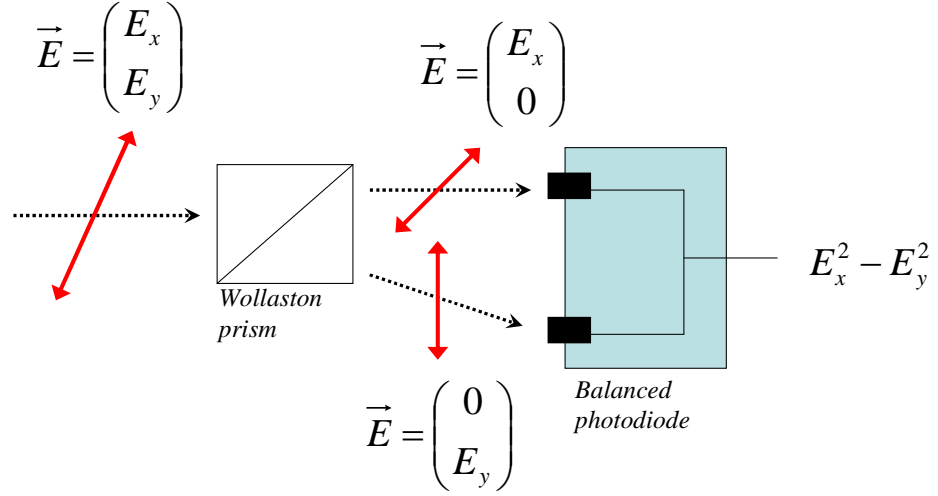


Figure 4.4: Diagram of balanced photodetection scheme

of values from the lockin to the computer, values are transferred as they are stored in the lockin and converted to real values by the computer. The lockin stores values as pairs of integers  $(a, b)$ , which are converted to decimal values by the expression:

$$value = a \times 2^{(24-b)}. \quad (4.19)$$

For measurements using the Clark scanning delay line, we connect the output from the lockin channel into a Lecroy oscilloscope, which is triggered on the 22 Hz signal from the position output of the Clark. The time trace of the Kerr signal results from averaging this trace on the scope. The position of the Clark is measured as a sinusoidal voltage on the scope, and this is averaged as well. The time-delay of the scan is calibrated by comparing the voltage amplitude of the Clark output with the distance moved by the Clark retroreflector, which is measured by finding the difference in step-motor position when the pump-probe  $t=0$  time is translated to either end of the the Clark motion.

#### 4.4.3 Derivative Measurements

For Fourier analysis of the time-resolved Kerr data, the numerical derivative of the time-trace was used to reduce windowing effects (see section 6.1). In order to eliminate the need to smooth the time-trace data and compute the derivative, derivative data on BiFeO<sub>3</sub>/SRO bilayer samples was measured experimentally.

To measure the derivative, a double lockin scheme is utilized. The output from the

lockin triggering on the PEM is sent to a second lockin that triggers on the Clark frequency. This is the same configuration as used when taking data with the Clark, only the second lockin replaces the oscilloscope. The Clark motion is reduced to a sub-picosecond amplitude of motion, and the time-dependence of the derivative is measured by stepping the Newport delay line. The Clark motion remains sinusoidal for amplitudes down to approximately 0.5 ps, becoming distorted for lower ranges of motion.

## 4.5 Cryostats

For magnetic measurements of the TR-MOKE, we used an Oxford SM-4 superconducting magnetic cryostat, capable of reaching fields up to 6T. The sample is cooled through a helium exchange gas introduced by a needle valve connected to the helium bath surrounding the superconducting magnet. The ability to separate the magnet bath from the sample space with the needle valve allows us to cool the sample with a magnetic field applied. Two temperature sensors mounted using indium foil were used to measure the temperature at the helium evaporator at the bottom of the sample chamber and on the copper sample mount. The SM-4 can theoretically reach temperatures of  $\sim 1.2$  K by pumping on the exchange gas. Heating by the laser pulse raises the sample temperature significantly higher than this, making running the cryostat at such low temperatures impractical. During experiments, the cryostat was run with the exchange gas at slightly higher than atmospheric pressure, with a minimum temperature of  $\sim 4$  K.

For DC-MOKE measurements and for TR-MOKE measurements where variation of the magnetic field was not required, the majority of the data was taken using a RC110 Cryo Industries cold-finger cryostat, with occasional use of a Janis ST-300MS cold-finger cryostat. In both cryostats, indium foil was used to increase thermal contact between the cold-finger and the copper sample mount. The Cryo Industries cryostat was equipped with temperature sensors on the cold-finger and on the sample mount, while the Janis system has only one sensor on the sample mount. Both systems consistently reached minimum temperatures of  $\sim 4$  K.

In all cryostats, the samples were mounted to a copper block with Apiezon N-type grease.

## 4.6 Optical Bleaching Effects

The signal out of the detector depends on both the rotation of the polarization and the amount of light reflected off of the sample. Optical bleaching refers to time-dependent changes in the polarization as a result of changes in the electron distribution in response to the pump pulse. The signal from this effect mixes with the signal from time-dependent changes in the polarization due to changes in the magnetization, obscuring the measurement of the magnetic response [51].

The balanced detector measures the rotation by taking a subtraction of two initially perpendicular polarizations. Referring back to equation 4.7, the quantity measured by the detector is  $S = 2Re[\epsilon_{xy}\epsilon_{xx}^*]$ . The change in the signal induced by the pump pulse is then

$$\Delta S = 2Re[(\Delta\epsilon_{xy})\epsilon_{xx}^* + \epsilon_{xy}(\Delta\epsilon_{xx}^*)]. \quad (4.20)$$

The first term in the sum represents the change in polarization, and the second represents the optical bleaching effect. The term  $\epsilon_{xy}$  gives the rotation due to the equilibrium magnetization. Optical bleaching is effectively a change in reflectivity that changes the amount of DC Kerr signal measured, giving an effective time-dependent polarization.

By making time-resolved measurements of the magneto-optical Kerr effect, ellipticity, and intensity of the reflection we can make inferences about the relative changes in  $\epsilon_{xx}$  and  $\epsilon_{xy}$ . In metallic systems, the dynamics of the change in reflectivity occur on a time scale of about 1 ps, and are due to the electron absorption of the laser energy and subsequent decay. In these systems, the signal on time-scales longer than 1 ps represent an accurate measure of the magnetization dynamics.

## 4.7 Exciting FMR in an Optical Experiment

Since Beaurepaire's first measurement, several schemes have been used to excite magnetic precession in time-resolved optical experiments. The most direct method is to apply a perturbing magnetic field. This has been accomplished on a picosecond time-scale through the use of photoconducting switches [34, 1], where the pump pulse opens a biased switch and generates a time-dependent current that results in a perturbing magnetic field.

The method relevant to exciting magnetization precession in SRO is a change in the magnetic anisotropy of the system in response to laser heating [93]. This all-optical excitation technique requires no circuitry, and the rise time is limited by the effective heating time of the system, which is typically less than the rise time of a current-driven magnetic

perturbation. Magnetic precession in thin films can be driven by the shape anisotropy, which changes in response to a thermally induced reduction in the magnetization. In SRO films, we utilize the intrinsic anisotropy rotation described in chapter 2.

## 4.8 Laser Excitations of the Magnetic System

The magnetic precession is generated by a change in anisotropy in response to heating of the sample by the laser pulse, so understanding the picosecond dynamics of the system requires that we understand the way the sample is heated on a picosecond time-scale. The laser pulse only deposits energy directly into the electrons through direct ( $k = 0$ ) dipole transitions and this energy is then spread to the lattice and spins through scattering processes. In the three temperature model, the electrons, spins, and lattice are considered as three separate thermal baths, where the bath energies are treated as effective equilibrium temperatures after the initial scattering processes [70].

The laser excites a small number of electrons with an energy of 1.5 eV, which is orders of magnitude above the thermal energy. The equilibrium concept of temperature is therefore not applicable to the early stages of laser excitation [52]. In metallic systems, there are a large number of available states around the Fermi energy, leading to a fast decay of the excited electrons. Electron-electron scattering between laser-excited electrons and thermal electrons creates a large number of “hot” electrons. This scattering redistributes the electron energy without changing the average energy of the electron bath, and the electrons are then considered to be in equilibrium at an elevated temperature  $T_e$ . Once a large number of a excited electrons is created in the system, energy transfer between electrons and phonons becomes more efficient, and the lattice temperature will subsequently come into equilibrium with the electron temperature. The timescale for electron thermalization is typically on the order of 100s of fs, and the electron-phonon equilibration time is  $< 1$  ps [89, 51].

### 4.8.1 Ultrafast Demagnetization

In TR-MOKE measurements, an immediate reduction in the magnetization has been observed in response to the pump-pulse, suggesting spin-flip scattering in the initial decay of electrons [5, 50]. Due to the short time-scales on which the ultrafast demagnetization occurs, measurement of the demagnetization is complicated in time-resolved optical measurements by optical bleaching effects described in section 4.6. Regardless of the difficulty in the measurement, the general consensus is that part of this signal is magnetic in

origin [50].

In the presence of spin orbit coupling, the spin up and spin down states are no longer good quantum states, and spin scattering can occur during the decay of excited electrons. The good quantum states are linear combinations of the spin up and spin down states, and spins are scattered in the electron decay due to this spin-state mixing [100, 19]. This initial spin randomization is referred to as ultrafast demagnetization, and leads to an initial higher spin effective temperature  $T_s$ .

This initial demagnetization has been shown to be dominated by avoided crossings in the band structure in Co thin films [78]. This process is thought to be the same as the process that enhances the electron-spin resonance line-width in Al. In many metals, the temperature dependence of the spin-relaxation time is the same, with the exception being metals with avoided crossings [24, 67]. Elliott-Yafet scattering is enhanced at points in the band structure where the conduction and valence bands are nearly degenerate, making the spin-scattering significantly faster [25].

## 4.9 Three Temperature Model

On time-scales longer than the electron-relaxation time, the perturbation is due to thermal effects, and is generally treated within the three-temperature model [101]. The coulomb interaction is responsible for the coupling between the electrons and the lattice, so in metallic systems, the temperature exchange between those two systems is generally faster than the temperature exchange between the spin system and the electron system, which comes about through spin-orbit coupling. Temperature exchange between the spin and the phonon system is usually described by spin-wave interactions with phonons. Experiments have shown evidence of magnon-phonon coupling in SRO, but in general this coupling term is thought to be weak [41].

The equations for heat flow between the three reservoirs are given by the following equations, with the term  $S(z, t)$  representing the source term describing the energy input into the electron system [92, 101]:

$$\begin{aligned}
C_e(T_e)\frac{\partial T_e}{\partial t} &= \frac{\partial}{\partial z} \left[ \kappa_e(T_e)\frac{\partial T_e}{\partial z} \right] - G_{eL}(T_e - T_L) - G_{es}(T_e - T_s) + S(z, t) \\
C_s(T_s)\frac{\partial T_s}{\partial t} &= \frac{\partial}{\partial z} \left[ \kappa_s(T_s)\frac{\partial T_s}{\partial z} \right] - G_{sL}(T_s - T_L) - G_{es}(T_s - T_e) \\
C_L(T_L)\frac{\partial T_L}{\partial t} &= \frac{\partial}{\partial z} \left[ \kappa_L(T_L)\frac{\partial T_L}{\partial z} \right] - G_{sL}(T_L - T_s) - G_{eL}(T_e - T_L).
\end{aligned} \tag{4.21}$$

Here, the z-direction is defined as the direction perpendicular to the sample plane. The heat capacity of the different reservoirs are represented by the variable  $C$ ,  $G$  represents the coupling between reservoirs, and  $\kappa$  represents the heat diffusion into the sample. The subscripts  $s$ ,  $e$ , and  $L$  refer to the spins, electrons, and lattice, respectively. In-plane diffusion can be included in the model by adding terms of the form,  $\frac{\partial}{r\partial r} (r\kappa\frac{\partial T}{\partial r})$ , but inplane flows can be neglected for thin film geometry. In metals, the Wiedemann-Franz law suggests that the heat diffusion is dominated by electrons, i.e.  $\kappa_e \gg \kappa_s, \kappa_L$ .

## 4.10 Specific Heat Contributions in Metals

The specific heats appearing in equations (4.21) are all temperature dependent. In non-magnetic metals, the electron specific heat dominates at low temperature, and the phonon contribution dominates at higher temperature. The magnetic contribution depends on the spin stiffness, and in ferromagnets with high transition temperatures, is small compared to the lattice specific heat.

The temperature dependence of the Fermi distribution function determines the temperature dependence of the electron specific heat in the free-electron model. The effect of thermal excitations on the electron distribution function is to smear out the distribution on an energy scale of  $k_B T$  around the Fermi level. Roughly, the number of electrons thermally excited by the fermi level is given by  $g(\epsilon_F)k_B T$ , where  $g(\epsilon_F)$  is the density of states at the Fermi energy [3]. The energy density is then  $g(\epsilon_F)(k_B T)^2$ , which gives a specific heat that is linear in temperature.

The lattice specific heat is dependent on the on the energy spectrum of the phonon normal modes, and the full temperature dependence is difficult to calculate. In the low temperature limit, the lattice specific heat can be calculated by considering only the linear contribution from the acoustic phonon modes. The low-temperature specific heat, with only the electron and phonon contributions, is given by the equation:

$$C = \frac{\pi^2}{2} \left( \frac{k_B T}{\epsilon_F} \right) n k_B + B T^3. \quad (4.22)$$

The linear term is the electron contribution, and the cubic term is the phonon contribution. Early reports suggest that the low-temperature specific heat of crystalline SrRuO<sub>3</sub> fits the form of (4.22), with a cross-over from electron to lattice specific heat occurring around 3K [2]. Later reports [14], as well as calculations of the specific heat based on our time-resolved measurements, indicate that above 10K, the magnon specific heat is dominant.

#### 4.10.1 Magnetic Specific Heat

The magnetic Hamiltonian in an isotropic system can be written in terms of an exchange energy,  $J$ , as:

$$H = - \sum_{i \neq j} J_{ij} \hbar^2 S_i \cdot S_j. \quad (4.23)$$

In magnetic systems, spins have strong short-range interactions encouraging parallel alignment from exchange coupling, and the ground state energy is the fully-aligned spin state. The elementary excitations above the ground state are spin-flips away from this fully aligned configuration. In the lowest-lying excited states, the spin-flip is shared over several spin sites, so that the gain in exchange interaction energy between each nearest-neighbor is small. The lowest excited state is therefore a linear combination of spin states, with a total of one reversed spin. These excited states are spin waves; the lowest energy excitations are quantized spin waves known as magnons.

At low temperatures the magnon spectrum is dominated by long-wavelength excitations, and the spin-waves can be defined through an approximate dispersion relation:

$$\hbar\omega = \gamma k^2, \quad (4.24)$$

where  $\gamma$  is the spin-wave stiffness.

At low temperature, the number of excitations is assumed to be small, and multiple magnon excitations can be treated as a superposition of single magnon excitations. By treating the magnons as a system of harmonic oscillators, the distribution of magnon energies can then be treated with Bose-Einstein statistics. The energy of the magnon system can then be calculated by integrating over the density of states and the Bose-Einstein distribution function:

$$\begin{aligned}
U &= \int_0^\infty \epsilon(k) D(k) \eta(k) dk \\
&= \int_0^\infty \epsilon(k) \eta(k) \frac{(4\pi k^2)}{(2\pi)^3} dk \\
&= \int_0^\infty \frac{\hbar\omega}{e^{\hbar\omega/k_B T} - 1} \left[ \frac{1}{4\pi^2 \omega} \left( \frac{\hbar\omega}{\gamma} \right)^{3/2} \right] d\omega \\
U &= \frac{1.783}{4\pi^2} \gamma^{-3/2} (k_B T)^{5/2}. \tag{4.25}
\end{aligned}$$

The internal energy, and therefore the specific heat, depends on the spin stiffness as  $C \propto \gamma^{-3/2}$ . In transition metal ferromagnets such as Fe and Co, the spin stiffness is on the order of hundreds of meV-Å<sup>2</sup>, which is large enough that the magnon specific heat contribution is negligible. The spin stiffness in SrRuO<sub>3</sub> is somewhat smaller than in these elemental magnets, as suggested by a lower transition temperature of around 150 K.

The above calculation of the magnetic contribution to the internal energy assumes an isotropic system, whereas SRO is marked by a large magneto-optic anisotropy. In the Ising model, the effect of this anisotropy is to add a term to the Hamiltonian, such that, with  $D$  representing the anisotropy, the Hamiltonian reads:

$$H = - \sum_{i \neq j} J_{ij} \hbar^2 S_i \cdot S_j + D \hbar^2 (S_z^i)^2. \tag{4.26}$$

The anisotropy changes the spin-wave dispersion relation to  $\hbar\omega = \gamma k^2 + \Delta\epsilon$ , where  $\Delta\epsilon = D\hbar^2/2$ . This creates a gap in the magnon density of states. Adjusting the equation for the magnetic internal energy to account for the anisotropy, equation 4.25 now reads:

$$U = \int_{\Delta\epsilon}^\infty \frac{\hbar\omega}{e^{\hbar\omega/k_B T} - 1} \left[ \frac{\sqrt{\omega - \Delta\epsilon/\hbar}}{4\pi^2} \left( \frac{\hbar}{\gamma} \right)^{3/2} \right] d\omega.$$

In SRO, for an anisotropy field of  $\approx 6$ T, the spin-wave gap corresponds to a temperature of about 12K.

We can calculate the deviation of the internal energy from the low-temperature limit by using a more complicated spin-wave dispersion relation, and keeping the harmonic oscillator approximation. Pesz and Munn calculated the density of states for rectangular and tetragonal lattices in the tight-binding model, considering only nearest-neighbor interactions [80]. A plot of the internal energy calculated by numerical integration is shown in figure 4.5. For moderate anisotropies, the tight-binding density of states deviates from the low-temperature limit ( $D(\omega)d\omega \propto \sqrt{\omega}d\omega$ ) at a temperature determined only by the spin stiffness

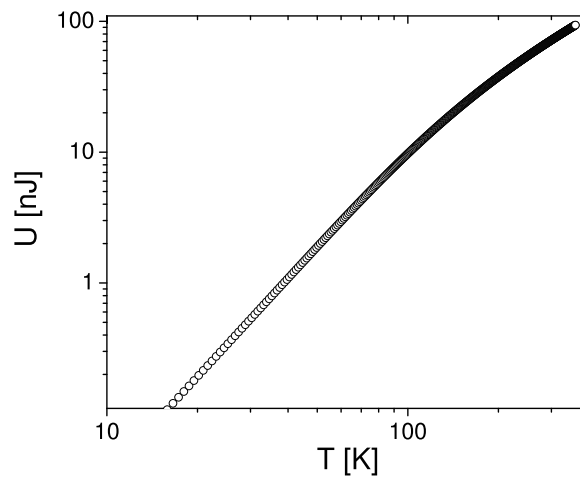


Figure 4.5: Calculated internal energy using the tight-binding model density of states

- changing the spin-stiffness in this calculation simply renormalizes the temperature axis. The deviation of the internal energy from  $T^{5/2}$  occurs at a temperature roughly two orders of magnitude below the exchange energy.

## Chapter 5

# Thermal Modeling of SRO Dynamics

The time-resolved change in Kerr angle of a 200 nm SRO thin film in response to a pump pulse is shown in figure 5.1 and can be separated into two temperature regimes. In the high temperature regime ( $90K < T < 150K$ ), the magnitude of the signal increases near  $T_C$ , and shows a slow rise time that also slows near  $T_C$ . As the sample is cooled below 90K, the signal again increases in magnitude, and damped oscillations with a period of 4 ps become clearly resolved at low temperatures. While the change in Kerr angle is measured as a positive value, these signals actually represent a reduction in the out-of-plane magnetization.

### 5.1 The Thermal Model and SRO

As will be discussed in chapter 6, the TR-MOKE signal oscillates in response a change in the anisotropy direction in response to laser heating. On time-scales longer than the electron-relaxation time, the perturbation is due to thermal effects and is generally treated within the three-temperature model [101]. As shown in figure 5.1, on the time-scale of the data the TR-MOKE time-traces are approximately constant after  $t \approx 15$  ps at all temperatures. On a time-scale of  $t > 15$  ps, the sample is in a quasi-equilibrium state, and the sample is slowly cooling by transferring heat to the substrate.

A plot of the quasi-equilibrium changes in the Kerr rotation is shown in figure 5.2. Since the magnetization dynamics are triggered by a thermal change in the anisotropy field,

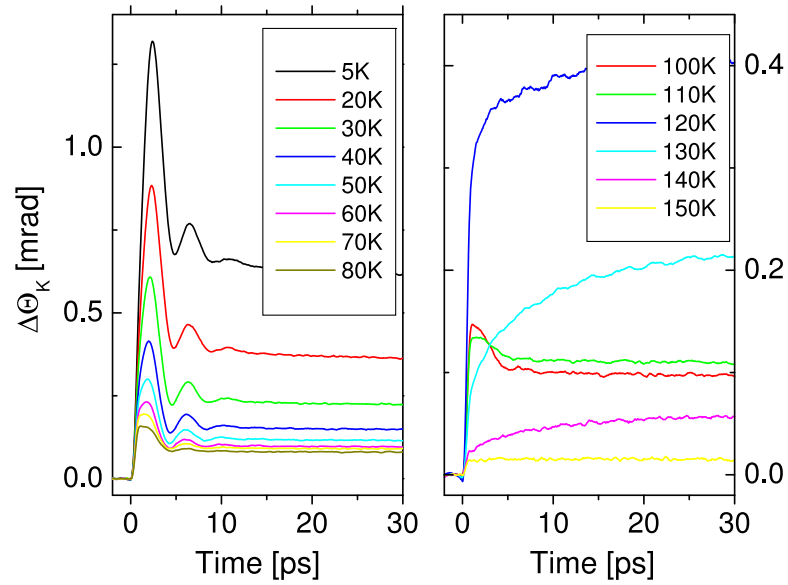


Figure 5.1: Change in Kerr rotation as a function of time delay following pulsed photoexcitation on a 200 nm SRO/STO film. Left Panel: Temperature range  $5K < T < 80K$ . Right panel: Temperature range  $100K < T < 150K$ .

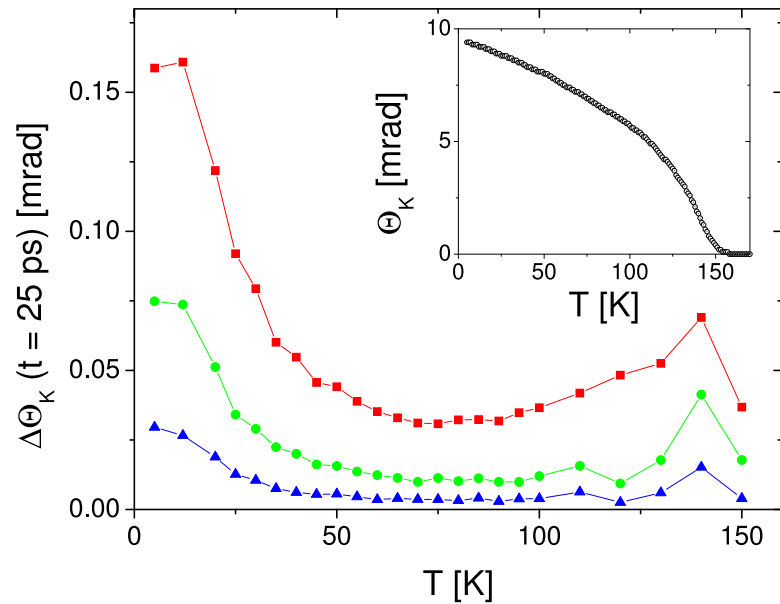


Figure 5.2: Change in Kerr rotation at  $t = 25$  ps as a function of temperature. Different line colors correspond to different pump fluences. The inset shows the Kerr angle as a function of temperature

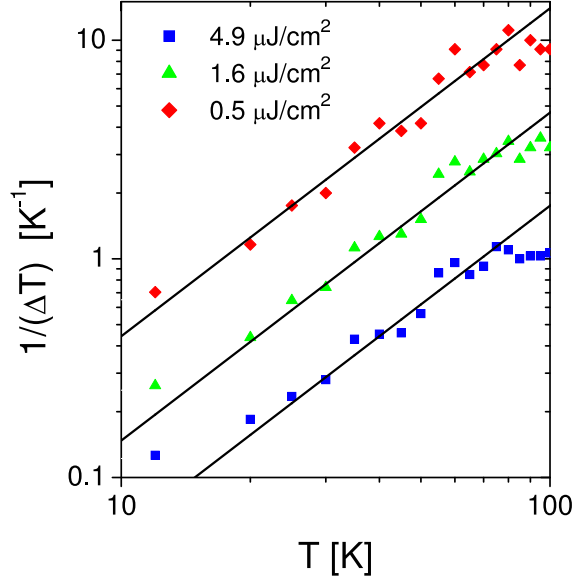


Figure 5.3:  $1/(\Delta T)$ , where  $\Delta T$  is the calculated change in temperature, plotted for difference pump fluences. The black lines are fits to  $T^{3/2}$

this long-lived change in the Kerr angle is given roughly by

$$\Delta M = \Delta T(dM/dT) = (\Phi/C(T))(dM/dT), \quad (5.1)$$

where  $\Phi$  is the pump pulse energy, and  $C(T)$  is the specific heat. The increase in the amplitude of the time-dependent Kerr signal at low temperature is a result of the decreasing specific heat, while the peak near  $T_C$  is caused by the increase in the slope of the magnetization temperature dependence near the transition.

We can measure the temperature increase in response to the pump pulse by comparing the change in TR-MOKE signal with the temperature dependence of the DC-MOKE signal. A plot of the DC-MOKE signal is shown as an inset to figure 5.2; the measured magnitude of the Kerr angle is consistent with previous reports [47]. The reciprocal of the measured change in temperature using this method for low pump powers is plotted in figure 5.3.

The energy deposited by the pump pulse is equal to the change in the internal energy of the sample, and for a pump power  $\Phi$ , this is determined by an integration over the specific heat:

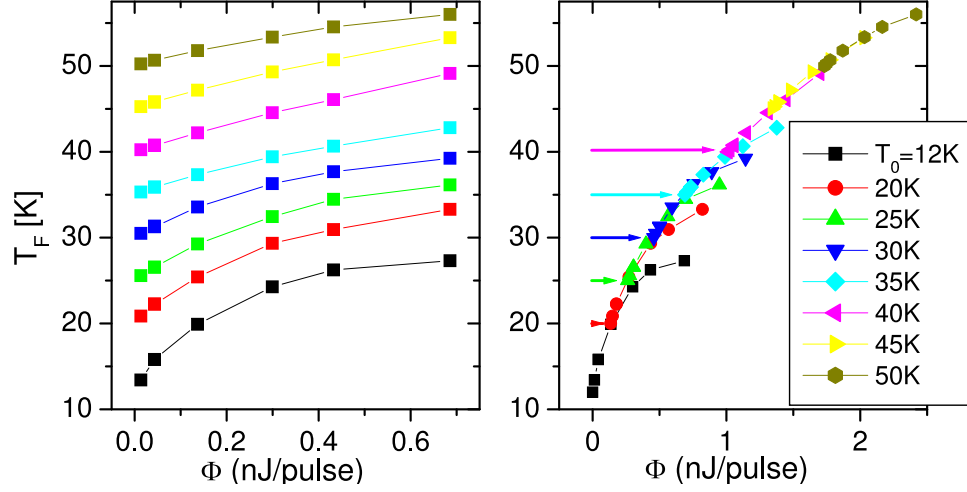


Figure 5.4: Left panel: Calculated  $T_F$  vs. pump pulse intensity for different values of the equilibrium sample temperature. Right panel: Data shifted to lie on a common curve.

$$\int_0^\Phi d\Phi = \int_{T_0}^{T_f} C(T)dT \quad (5.2)$$

$$= U(T_f) - U(T_0). \quad (5.3)$$

For low pump powers, the change in temperature can be treated in the linear approximation ( $C(T)dT = d\Phi$ ), and the functional form of the specific heat can be measured through the temperature dependence of the sample response at low laser power. The  $1/\Delta T$  data plotted in figure 5.3 show a  $T^{3/2}$  temperature dependence up to  $\sim 80\text{K}$ , indicating that below this temperature, the specific heat is dominated by magnons. We attribute the deviation from a  $T^{3/2}$  temperature dependence at  $80\text{K}$  to the deviation from the low-temperature approximation of  $\epsilon^{1/2}$  for the magnon density of states.

Higher pump intensities can be analyzed by using the full expression for the final temperature in terms of the internal energy:

$$T_F = U^{-1}(U(T_0) + \Phi). \quad (5.4)$$

The effect of changing the sample temperature,  $T_0$ , for a signal vs. intensity scan is to shift the  $T$  vs.  $U^{-1}$  function along the x-axis by an amount  $U(T_0)$ . Each  $T_F$  vs. intensity curve can be shifted along the intensity axis to lie along a common line that represents the full  $T_F$  vs. intensity curve, and the shifting amount along the x-axis should be consistent with

$U(T_0)$ . This shifting scheme is diagrammed in figure 5.4. At lower sample temperatures ( $T \leq 35K$ ), data points from high laser intensities deviate from the common  $T$  vs.  $\Phi$  line because the laser pulses induce enough heating of the sample that the temperature sensor on the cryostat mount no longer accurately reflects the equilibrium sample temperature. This DC heating becomes negligible at high temperatures due to the increased specific heat of the system.

The results of the shifting procedure are shown in figure 5.5. The data indicate a  $T^{5/2}$  temperature dependence up to about 80K, consistent with the  $T^{3/2}$  temperature dependence in figure 5.3. The right panel shows the calculated internal energy plotted versus  $T^{5/2}$  for samples of different thicknesses. The results of this more careful analysis supports the conclusion that the internal energy is dominated by magnons over a wide range of temperature. As expressed in equation (4.25), the slope of this line ( $m$ ) is then directly related to the spin stiffness, as

$$\gamma = \left[ \frac{1.783 L}{4\pi^2 m} \right]^{3/2}, \quad (5.5)$$

where  $L$  represents the effective diffusion length of energy into the sample.

### 5.1.1 Normalization of Laser Pulse Energy

We can calculate the functional form of the internal energy of the sample by knowing only the pump-pulse power, but to calculate the spin stiffness, we need to calibrate the density of the energy deposited in the sample. The time-resolved response is thermal in nature, but since the specific heat is generally a function of temperature, the thermal response will be nonlinear in the laser power. This leads to corrections due to the spatial profile of the deposited energy,  $\phi(r, z)$ , and due to the time-dependent nature of the pump laser power. The energy distribution in the sample plane ( $\phi(r)$ ) can be measured, and the distribution in time is straight-forward to calculate. The depth profile of the energy ( $\phi(z)$ ) is time-dependent, and determined by the penetration depth and the diffusion of the laser energy into the sample. As a result, figure 5.5 is plotted as function of pump fluence, and not the deposited energy density. The normalizations needed to account for the in-plane spatial profile and time-dependence of the pump are discussed below. The diffusion is discussed in detail in section 5.2.

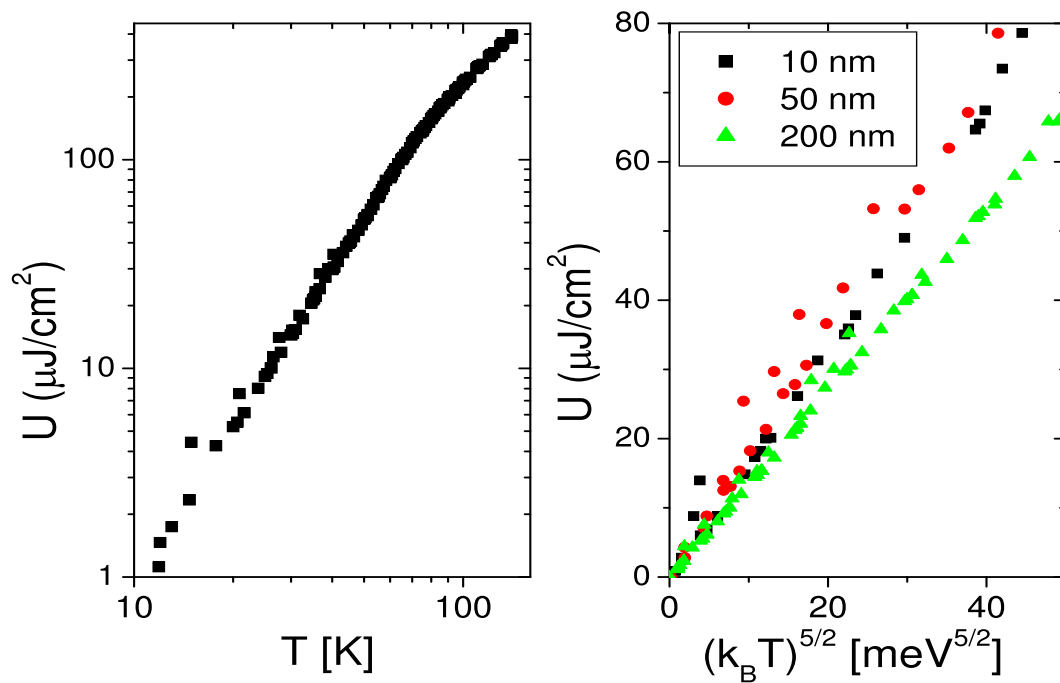


Figure 5.5: Left panel: Log-Log plot of the calculated internal energy vs. temperature for a 200nm SRO sample. Low temperature data fits at  $T^{5/2}$  temperature dependence. Right panel: Calculated internal energy for 10nm, 50nm, and 200nm thick samples, plotted vs.  $k_B T^{5/2}$

### In-plane Spatial Profile

The temperature rise under the laser spot is non-uniform, due to the Gaussian profile of the pulse in the sample plane. The spatial profile in the sample plane is:

$$\phi(q) = \phi_{q,p} e^{-r^2/(2\sigma^2)}. \quad (5.6)$$

We measure the spatial width of the laser pulse by using a razor blade on a translation stage with a micrometer, and also by measuring the amount of power transmitted through pinholes of various sizes. The diameter of the pump pulse is measured as  $2\sigma \approx 50 \mu\text{m}$ . The energy density of the pulse is given by  $\phi_{q,p}$ , where  $q$  corresponds to the probe intensity,  $p$  to the pump.

The measured final magnetization is given by an integral of the final magnetization profile over the probe laser profile:

$$\overline{M}_F = \int_0^R 2\pi r \phi_q f(r) M(U^{-1}(\phi_p f(r) + U(T_0))) dr. \quad (5.7)$$

The integral is taken up to a radius  $R$ , which is a cut-off determined by an iris placed in between the sample and the detector. To evaluate the integral, we introduce a function  $G$ , such that  $\frac{dG(\phi)}{d\phi} = M(U^{-1}(\phi))$ , and a change of variables  $y = \phi_p f(r)$ :

$$\begin{aligned} \overline{M}_F &= \frac{2\pi\sigma^2\phi_q}{\phi_p} \int_{\phi_p f(R)}^{\phi_p} M(U^{-1}(y + U(T_0))) dy \\ &= \frac{2\pi\sigma^2\phi_q}{\phi_p} [G(\phi_p + U(T_0)) - G(\phi_p f(R) + U(T_0))]. \end{aligned} \quad (5.8)$$

The data is normalized by the the probe power, which is given by:

$$\begin{aligned} \Phi_q &= \int_0^R 2\pi r \phi_q f(r) dr \\ &= 2\pi\sigma^2\phi_q(1 - f(R)). \end{aligned} \quad (5.9)$$

Dividing equation 5.8 by equation 5.9 gives:

$$\begin{aligned} \overline{M}_F &= \frac{1}{\phi_p(1 - f(R))} [G(\phi_0 + U(T_0)) - G(\phi_p - \phi_p(1 - f(R)) + U(T_0))] \\ &= \frac{1}{\Gamma\phi_p} [G(\phi_p + U(T_0)) - G(\phi_p - \Gamma\phi_p + U(T_0))]. \end{aligned} \quad (5.10)$$

where  $\Gamma = 1 - f(R)$  is a measure of the fractional probe power passed through the iris. In the limit of  $R \rightarrow 0$ ,  $\Gamma \rightarrow 0$ , and equation 5.10 reduces to a derivative, giving:

$$\overline{M_F} = M(U^{-1}(\phi_p + U(T_0))). \quad (5.11)$$

For small enough  $R$ , the measurement is insensitive to the radial energy profile of the pulse when normalized by the probe intensity. This derivative approximation is valid in the regime given by:

$$\Gamma \ll \frac{U(T_0) + \phi_p}{\phi_p}. \quad (5.12)$$

During experiments, the iris is closed such that the probe power is reduced to approximately 20 percent of the maximum ( $\Gamma = 0.2$ ), which corresponds to  $R = 0.67\sigma$ . For this value of  $\Gamma$ , the derivative approximation is roughly valid when the pump pulse energy density is less than the internal energy of the sample at the equilibrium temperature.

### Normalization of Lockin Response

The nonlinearity in the magnetic response leads to an adjustment factor of the signal value due to the time-dependence of the pump intensity. The chopped laser intensity has a functional form  $\cos^2(\omega t)$ , but the non-linearity of the magnetic response alters the measured Kerr-angle time-dependence. The lockin reads the signal at a frequency of  $2\omega$ , as described in section 4.2, so if we define  $x = \omega t$ , the response measured on the lockin is given by:

$$\begin{aligned} \Theta_K &= \frac{1}{2\pi} \int_0^{2\pi} \cos(2x) U^{-1}[\phi(x) + U(T_0)] dx \\ \phi(x) &= \phi_p \cos^2(x). \end{aligned} \quad (5.13)$$

To get the correction due to the nonlinearity in the temperature response to the laser, we assume a temperature dependence of the internal energy  $U(T) = \alpha T^\beta$ . This gives

$$\begin{aligned} U^{-1}(\phi(x) + U(T_0)) &= \frac{1}{\alpha^{1/\beta}} (\phi(x) + U(T_0))^{1/\beta} \\ &= \left(\frac{U(T_0)}{\alpha}\right)^{1/\beta} \left(\frac{\phi(x)}{U(T_0)} + 1\right)^{1/\beta} \\ &\approx \left(\frac{U(T_0)}{\alpha}\right)^{1/\beta} \left(1 + \frac{1}{\beta} \frac{\phi(x)}{U(T_0)}\right). \end{aligned} \quad (5.14)$$

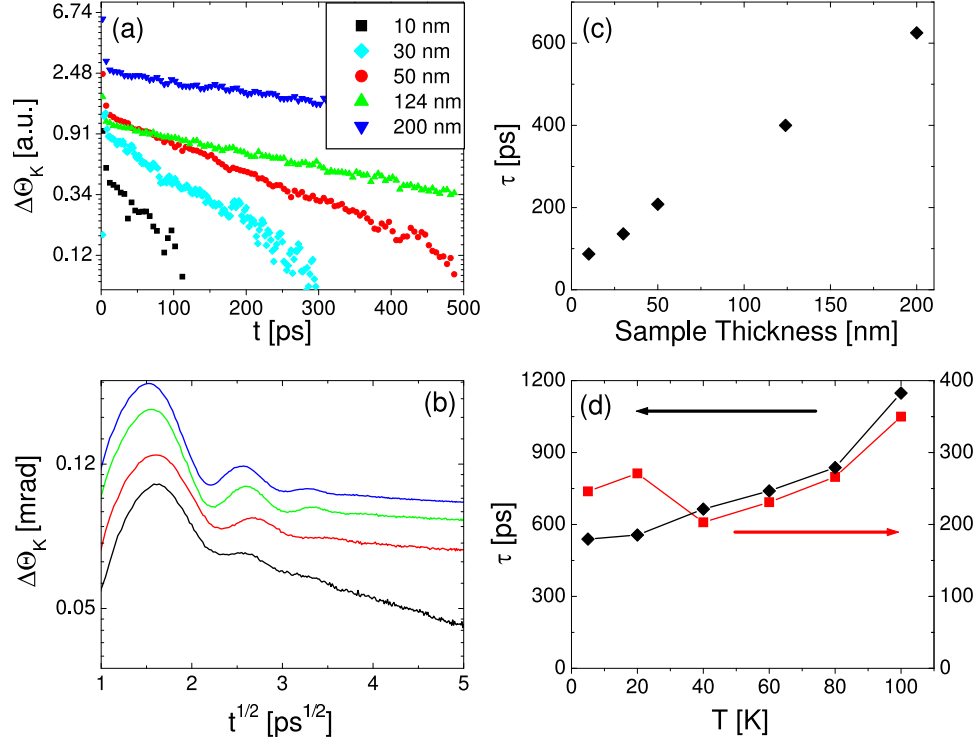


Figure 5.6: (a) Semi-log plot of 500 ps TR-MOKE signals for samples of various thickness. (b) Log of short time ( $t < 25$  ps) TR-MOKE signal plotted against  $t^{1/2}$ , indicating stretched exponential behavior. (c) Decay times plotted versus sample thickness. (d) Decay times versus temperature for 200 nm (black, left axis) and 50 nm (red, right axis) films.

On the last line, we again assume that  $\phi(x) \ll U(T_0)$ , and keep only the linear term in the expansion. The first term in the expansion is constant in time, and doesn't contribute to the lockin reading. The lockin reading for the second term is:

$$\Theta_K = \frac{(U(T_0))^{(1-1/\beta)}}{2\pi} \int_0^{2\pi} \cos(2x) \left( \frac{1}{\beta} \cos^2(x) \right) dx. \quad (5.15)$$

This result differs from the pure  $\cos^2(x)$  lockin value by a factor of  $1/\beta$ . For the case when magnons dominate the internal energy,  $\beta = 5/2$ .

## 5.2 Heat Transfer Into the Substrate

In order to study the diffusion of heat into the sample and the transfer of heat from the sample to the substrate, we studied a series of sample thicknesses on a time-scale of 500 ps. The one-dimensional diffusion in terms of the specific heat  $C$  and thermal conductivity

$\kappa$  is given by [13]:

$$\frac{1}{C} \frac{\partial T}{\partial t} = -\frac{\partial}{\partial z} \left( \kappa \frac{\partial T}{\partial z} \right). \quad (5.16)$$

Here  $z$  is the represents the distance from the sample surface. This equation is general for a position dependent  $\kappa$ . If  $\kappa$  is position independent, an analytical solution for an initial temperature distribution of a delta-function at  $t = 0$  and  $z = 0$  can be written as:

$$T(z, t) = \frac{1}{\sqrt{4\pi Dt}} e^{-\frac{z^2}{4Dt}}, \quad (5.17)$$

where  $D = \kappa/C$  is the thermal diffusivity. This expression can be generalized for different initial conditions by convolving the initial temperature distribution  $T_0(z, t = 0)$ , with the delta function solution given by equation (5.17). Solutions of this type should obey the boundary condition that no heat is transferred out of the sample at the sample surface, represented mathematically by  $\partial T/\partial z|_{z=0} = 0$ . This condition can be satisfied by treating the problem as symmetric about  $z = 0$ . Generalized solutions of equation (5.17) have an asymptotic time-dependence of  $T \propto t^{-1/2}$ .

Time-traces for TR-MOKE signal are shown on two different time-scales in figure 5.6, and there is no indication of a  $t^{-1/2}$  time-dependence. A semi-log plot of TR-MOKE on a scale  $t < 500$  ps is shown in figure 5.6a, showing an exponential decay that becomes faster with decreasing sample thickness. A plot of the decay times is shown in figure 5.6c, and shows a linear dependence of the decay time on the sample thickness ( $\tau \propto L$ ). A plot of the TR-MOKE signal on a shorter time-scale is shown in figure 5.6b. This short-time data indicates a stretched exponential, with a functional form of  $\exp[-(t/\tau)^{1/2}]$ .

A stretched exponential indicates a distribution of decay rates, such that the functional form of the decay is given by [6, 77]:

$$I(t) = e^{-(t/\tau_0)^\beta} = \int_0^\infty H(k) e^{-kt} dk, \quad (5.18)$$

where  $k$  represents the decay rate, and  $H(k)$  is the distribution. The analytical form of  $H(k)$  with  $\beta = 1/2$  is given by:

$$H(k) = \frac{\tau_0}{2\sqrt{\pi}(k\tau_0)^{3/2}} \exp\left(-\frac{1}{4k\tau_0}\right). \quad (5.19)$$

This type of decay has been observed in glass-like and disordered systems, and calculations on heat-transport in gold nano-particles have predicted stretched-exponential decays of the nano-particle temperature when cooling to a surrounding fluid [77, 38].

The exponential decays on longer time-scales, combined with the linear dependence of the decay times on the sample thickness, suggest a more straight-forward interpretation

of heat flow limited by a thermal boundary resistance between the SRO film and STO substrate [12, 91]. The thermal boundary resistance is a result of phonon reflection at the interface, and two theories exist to explain this reflection: the acoustic mismatch model and the diffuse mismatch model. The acoustic mismatch model is valid for cases with the phonon wavelength is longer than the atomic spacing; the phonons are treated as waves and reflect in response to differences in the phonon impedance on either side of the interface. This situation is effectively the phonon analogue to optical reflection and transmission. The diffuse mismatch model assumes complete scattering of the phonons at the interface. The transmission of phonons across the interface is determined by Fermi's golden rule, and the boundary resistance occurs due to a mismatch in the phonon density of states on either side of the interface.

If the temperature decay is limited by thermal boundary resistance, and the internal energy is dominated by phonons, the decay time is roughly independent of temperature. The amount of energy carried out by transmitted phonons and the total energy of the phonons in the film both scale the same way with temperature. The temperature dependence of the decay times of the TR-MOKE data, shown in figure 5.6d, seems consistent with this picture. However, as discussed in section 5.1, the thermal energy in SRO is dominated by magnons. The energy of the phonons that carry the heat out therefore has a different temperature dependence than the energy of the system as a whole, and a stronger dependence on temperature is expected in the decay times.

It has been suggested that there is an effective boundary resistance due to non-equilibrium between different temperature baths in a region near the film/substrate interface [60, 39]. The non-equilibrium region is a result of different boundary conditions for the different baths. Neither the electrons or the magnons can diffuse into the substrate, giving the condition that the slope of the temperature must vanish at the interface ( $\partial T/\partial z|_{z=L} = 0$ ). In the absence of a phonon-reflection type boundary resistance, the requirement for phonons at the substrate is that the heat flows on either side of the boundary must be consistent ( $\kappa_f \partial T_f/\partial z|_{z=L} = \kappa_s \partial T_s/\partial z|_{z=L}$ ). This leads to a region of non-equilibrium, characterized by a length scale  $\delta$  given by:

$$\delta = \sqrt{\frac{\kappa_p}{G}}, \quad (5.20)$$

where  $\kappa_P$  is the phonon thermal conductivity, and  $G$  is the coupling coefficient between electrons and phonons. This expression assumes that the electron thermal conductivity is much higher than that of the phonons. The thermal conductance across this region is given

by  $\kappa_p/\delta$ . This leads to an effective thermal boundary resistance, with a decay time given by:

$$\tau = \frac{CL}{G\delta} = \frac{CL}{\sqrt{\kappa_p G}}. \quad (5.21)$$

The temperature dependence of this decay depends on the temperature dependences of  $G$ ,  $\kappa_p$ , and  $C$ . The relevant specific heat is that of the magnons, and at low temperatures, the  $T$ -dependence of  $C$  ( $\sim T^{3/2}$ ) and  $\kappa_p$  ( $\sim T^3$ ) roughly cancel.

### 5.3 Finite-Difference Modeling

We attempt to describe the time-dependence of the SRO temperature by using a Dufort-Frankel finite difference scheme to model the heat flows described in the three temperature model expressed in equation (4.21) [20]. The three-temperature model implicitly assumes that the heat transfer is diffusive, which is a questionable assumption for film thicknesses on the order of 10 nm. For thicker films, this model does provide insight into the dependence of the time-evolution of the film temperature on various thermal parameters.

To mathematically model a thermal boundary resistance in equation (5.16) or in the phonon transport equation in (4.21), a term  $\delta(z = L)\frac{1}{R_S}(T_f - T_s)$  is added to the right-hand side, where  $R_S$  is the thermal boundary resistance,  $T_s$  and  $T_f$  are the temperatures of the film and substrate at the interface, and  $\delta$  is the Dirac delta function. In the finite-difference scheme, this results in a modification of the phonon boundary condition at  $z = L$ .

The finite-difference equation for the phonon heat flow from equation (4.21) is given by:

$$\begin{aligned} C_p \frac{T_p(j+1, k) - T_p(j-1, k)}{2\Delta t} &= \kappa_p \left[ \frac{T_p(j, k+1) - T_p(j+1, k)}{(\Delta z)^2} \right] \\ &\quad - \kappa_p \left[ \frac{T_p(j-1, k) - T_p(j, k-1)}{(\Delta z)^2} \right] \\ &\quad + G_{sp} [T_s(j+1, k) - T_p(j+1, k)] \\ &\quad + G_{ep} [T_e(j+1, k) - T_p(j+1, k)]. \end{aligned} \quad (5.22)$$

Here  $j$  is the time index, and  $k$  is the space index. There is an equation like this for each of the three thermal baths, and the temperature of each bath is advanced in time by solving the three algebraic equations for  $T_s(j+1, k)$ ,  $T_e(j+1, k)$ , and  $T_p(j+1, k)$ . To make the calculation more efficient, while still retaining detail of the temperature profile at the interface and modeling a substrate orders of magnitude thicker than the film, the spatial

step ( $\Delta z$ ) was small near the interface, and increased deep into the substrate. Changes in  $\Delta z$  were accounted for by using a non-symmetric derivative method [31].

Given that SRO is metallic and the specific heat is magnon-dominated, the following assumptions about the parameters were used in the modeling (see section 4.9):

$$\begin{aligned}\kappa_e &\gg \kappa_p; \kappa_s = 0 \\ C_s &\gg C_p \gg C_e \\ G_{ep} &\gg G_{es} \gg G_{sp}.\end{aligned}\tag{5.23}$$

The results of these simulations indicated that due to the relatively large spin specific heat, and the high electron thermal conductivity, the electrons and spins could be treated as one fluid. Simulations also showed decay times with the functional dependencies predicted by equation (5.21), but exponential decays were only seen when the phonon thermal conductivity was higher than that of the phonon in the film. Based on room-temperature thermal conductivity data, this assumption is not entirely unreasonable [96].

## Chapter 6

# TR-MOKE on SRO - Magnetization Dynamics

### 6.0.1 Critical Slowing Down

At temperatures above 80K, the data show dynamics consistent with those reported earlier [70]. The signal magnitude peaks around 120K, and as stated previously by Ogasawara, shows slow dynamics consistent with critical slowing down near the transition temperature. The peak in magnitude is consistent within a thermal model interpretation as the change in magnetism with temperature becomes steeper near the transition temperature.

The slow dynamics near the transition can be explained using dynamic scaling theory [42, 17]. Materials near a second-order ferromagnetic phase transition exhibit a scaling behavior; the statistical representation used to describe a system of individual spins can also be used to describe a system of blocks of spins, with the appropriate rescaling of the effective spin-spin coupling. As a result of this type of rescaling, relevant parameters near the transition temperature exhibit power-law behavior. The correlation length describes the length over which the system is ordered and diverges as the system approaches the transition temperature. The correlation length is related to the transition temperature through the critical exponent  $\nu$ :

$$\xi = (1 - T/T_C)^{-\nu}. \quad (6.1)$$

Dynamic scaling theory links the correlation length to the relaxation time by  $\tau = \xi^z = (1 - T/T_C)^{-\nu z}$  [90], which implies that the relaxation time, with the correlation length,

diverges at the transition temperature. The slow-time scales seen in the magnetization dynamics measurements can be interpreted as a divergence of the relaxation time of the system from an ordered state into a disordered state.

## 6.1 Magnetic Precession - Fourier Analysis

To analyze the oscillatory component of the data at low temperature, we take the Fourier transform (FT) of the numerical derivative of the time traces. The purpose of taking the derivative is to reduce windowing effects when calculating the discrete Fourier transform. The computer sums the FT from  $t = 0$  to the maximum time delay,  $t_{max}$ , in effect interpolating the signal to zero everywhere outside of the measured time window:

$$f(\omega) = \sum_{t=0}^{t_{max}} e^{-i\omega t} f(t) \Delta t. \quad (6.2)$$

In general, the decay of the time-traces is significantly slower than the time window captured by the Clark motion. This gives a large mean-value over the time trace, and results in a ringing of frequency  $1/t_{max}$  on the FT. The decay of the time traces being slow, the derivative is nearly zero at  $t = t_{max}$ , and interpolation of the derivative to zero beyond the time window does not result in ringing of the FT. As a result of the derivative, the analyzed function in frequency space is therefore  $i\omega f(\omega)$ . The resonant response is associated with the real part of the FT, so the relevant quantity is the imaginary part of the transform after the derivative  $Im [i\omega f(\omega)] = \omega Re [f(\omega)]$ .

To give cleaner transforms, we apply a Savitzky-Golay smoothing function to the time-traces before calculating the derivative. Applying a smoothing filter is essentially equivalent to increasing the time constant of the lockin during data collection, smoothing the high-frequency noise while reducing time resolution. The Savitzky-Golay filter performs a point-by-point polynomial regression analysis to generate the smoothed function [82]. This filter is desirable over a simple moving-average in that it preserves causality; the filtered point at a time  $t_n$  depends only on times  $t < t_n$ . The derivatives and FTs for the data in figure 5.1 up to 90K is shown in figure 6.1. A well-defined resonance peak is evident, becoming less well-defined at the sample is heated.

To confirm that the low-temperature oscillations are magnetic in origin, as opposed to another photoinduced periodic phenomenon such as strain waves, we measured TRMOKE dynamics in magnetic fields up to 6T. Figure 6.2 shows the time traces and associated Fourier transforms for the photoinduced dynamics in various fields. The frequency of the

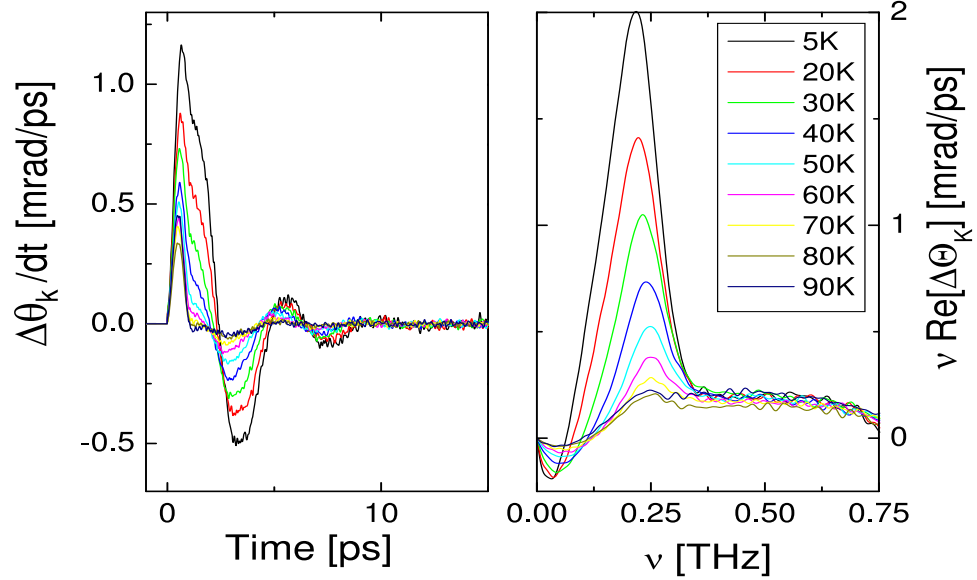


Figure 6.1: Left Panel: Numerical derivatives of TR-MOKE time traces. Right Panel: Fourier transforms of derivatives.

resonance peak increases with magnetic field as expected for ferromagnetic resonance. The inset in the right panel of the figure shows  $\Omega_{FMR}$  as a function of applied magnetic field. The solid line through the data points corresponds to an anisotropy field  $|\mathbf{h}_A| = 7.2$  T (for  $g = 2$ ) and easy axis direction equal to  $30^\circ$  from the film normal at 5K, consistent with previous determinations of  $\mathbf{h}_A$  based on equilibrium magnetization measurements [44, 62].

The origin of these oscillations is consistent with a sudden change in the direction of the easy axis in response to the pump pulse. The change in easy axis is due to the temperature-dependent change in the magneto-crystalline anisotropy axis and is caused by rapid laser-pulse induced heating [44]. From the thermal analysis in chapter 5, the perturbation in  $\mathbf{h}_A$  that we observe is consistent with a small rotation (on the order of  $1^\circ$ ). Before photoexcitation,  $\mathbf{M}$  is oriented parallel to the magnetic anisotropy  $\mathbf{h}_A$ . In the resulting non-equilibrium state,  $\mathbf{M}$  and  $\mathbf{h}_A$  are no longer parallel, generating a torque that induces  $\mathbf{M}$  to precess at the FMR frequency. In the presence of Gilbert damping,  $\mathbf{M}$  spirals towards the new  $\mathbf{h}_A$ , resulting in the damped oscillations of  $M_z$  that appear in the TRMOKE signal.

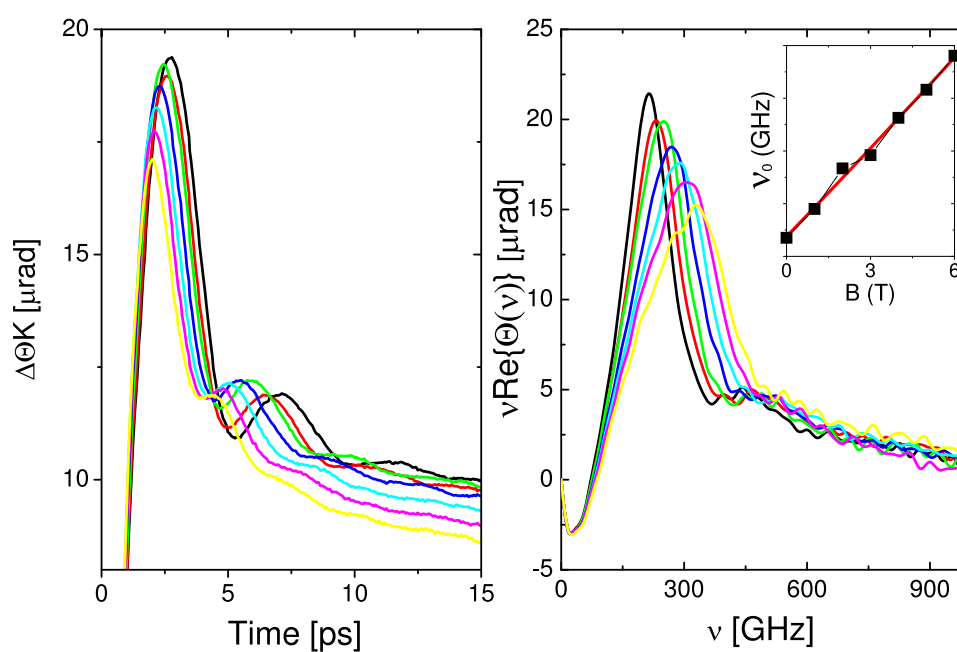


Figure 6.2: Left panel: Change in Kerr rotation as a function of time delay following pulsed photoexcitation at  $T=5$  K, for several values of applied magnetic field ranging up to 6 Tesla. Right panel: Fourier transforms of signals shown in left panel. Inset: FMR frequency vs. applied field. The fitted line is consistent with a  $g$  factor of 2.

## 6.2 Components of Magnetic Response

The TR-MOKE data and Fourier transform show more complicated structures than a simple resonant response expected from the LLG equation. In addition to the resonance peak in the Fourier transforms, the data in figures 6.1 and 6.2 show a negative peak at low frequency, and the derivatives of the time-traces show clear features of non-oscillatory behavior for times shorter than a picosecond. Although the spectra in figure 6.2 are clearly associated with a resonant response, the negative peak in the FT line-shapes is not consistent with a pure resonant response which gives a positive-definite Fourier transform. This negative peak is always present in the data, and is not the result of errors in assigning the zero-time of the time trace, which determines the phase of the FT.

In order to determine the physical processes that lead to these features of the FT line-shapes, we calculate the line-shapes while tuning the variables of the magnetic response - the sample temperature, external magnetic field, and the laser intensity. The features of interest are the resonant peak (RP) centered at  $\nu \approx 220$  GHz, the low-frequency negative peak (NP) at  $\nu \approx 40$  GHz, and the wide, high-frequency peak (HFP) at  $\nu \approx 500$  GHz. The FTs as a function of temperature are plotted in the right panel of figure 6.1, and the magnitudes of the different peaks vs. temperature are plotted in the left panel of figure 6.3. The amplitude of NP and RP both change dramatically with temperature, as does the frequency at the peaks. As shown in figure 6.3, the changes in the magnitudes of these two peaks show a similar dependence on temperature. The temperature dependence of the size of the HFP is much weaker.

The right panel of figure 6.3 shows the dependence of the FT line-shapes on pump intensity. The magnitude of the line-shapes are normalized by the pump intensity. The HFP appears constant with laser intensity on this plot, indicating a linear dependence of the HFP on intensity. The other two peaks both shift lower in frequency with decreasing pump intensity, while the magnitude of the RP shows a sub-linear response to laser intensity, as indicated by an increase of the normalized value.

The temperature and intensity dependence of the Fourier line shapes suggest that the NP and RP are part of the same phenomenon, while the HFP has a different origin. Additionally, the magnetic field data plotted in figure 6.2 suggests that the RP is magnetic in origin. Hence the NP and the RP both appear to be the result of precessional dynamics. The properties of the HFP are consistent with a photoinduced change in reflectivity due to band-filling, described in section 4.6.

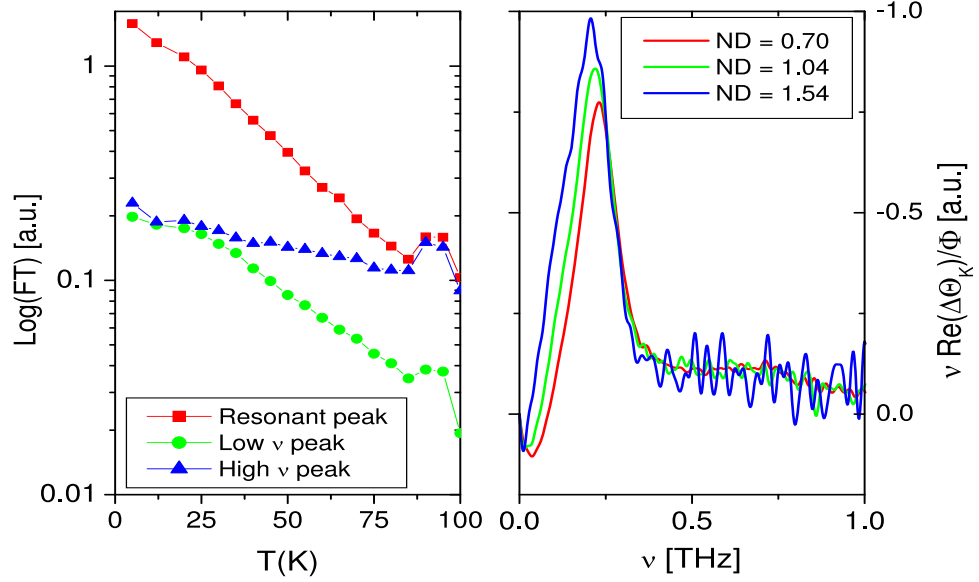


Figure 6.3: Left panel: Magnitudes of Fourier peaks as a function of temperature. Right panel: FT line-shapes normalized by pump intensity for several values of pump intensity at 5 K.

### 6.3 Modeling with linear response theory

To describe the magnetic response, the time-dependent magnetization is modeled using linear response theory:

$$\Delta M_i(t) = \int_0^\infty \chi_{ij}(\tau) \Delta h_A^j(t - \tau) d\tau. \quad (6.3)$$

In this equation,  $\chi_{ij}$  is the susceptibility and  $\Delta h_A^j$  is the change in anisotropy direction. By Fourier transforming the magnetic response, the convolution between  $\chi$  and  $\Delta h_A$  becomes a simple product of the individual Fourier transforms. Since the anisotropy direction is rotation as a function of temperature, we take a coordinate system such that  $\chi_{ij}$  represents the transverse susceptibility.

In the simple LLG case,  $\Delta h_A$  is a step function at  $t = 0$ , and the functional form of the response is determined by the susceptibility,  $\chi(\omega)$  given by[33, 65]:

$$\chi(\omega) = \frac{\chi(0)}{\omega - \omega_0 + i\alpha\omega_0}. \quad (6.4)$$

This function is peaked about the resonant frequency  $\omega_0$ , with a peak width given by the damping parameter  $\alpha$ . As discussed in the previous section, the resonance peak and low-

frequency negative peak are part of the same effect, so a simple peaked function described by equation (6.4) is insufficient to describe the dynamics.

### 6.3.1 The Overshoot Model

The TRMOKE signal is described well by modeling the anisotropy direction as time-dependent after  $t=0$ , instead of assuming a simple step function. We model the time-dependence of the anisotropy direction,  $\Delta h(t)$ , as a step function plus a decaying exponential, such that the anisotropy direction 'overshoots' the higher-temperature equilibrium direction. The time-dependence of the anisotropy direction is given by:

$$\Delta h(t) = \Theta(t)(\phi_0 + \phi_1 e^{-t/\tau_D}). \quad (6.5)$$

We consider the laser heating to be nearly instantaneous, and model the onset of the change in anisotropy with a step function at  $t=0$ , given by  $\Theta(t)$ . In further analysis we will ignore this function and implicitly assume a time-domain of  $t > 0$ . The direction of the easy axis at  $t=0$  is given by the value  $\phi_0 + \phi_1$ . The easy axis then asymptotically approaches the value  $\phi_0$  with a decay time given by  $\tau_D$ . The magnitude of the step function  $\phi_0$  represents the size of the equilibrium change in anisotropy, and the value  $\phi_1$  represents the amount by which the anisotropy direction overshoots the equilibrium.

The Fourier transform of (6.5) is

$$\phi(\omega) = \frac{\phi_0}{i\omega} + \frac{\phi_1}{1/\tau - i\omega}, \quad (6.6)$$

. and the total response is then given by:

$$\phi(\omega) = \frac{\chi(0)\phi_0}{i\omega} \left( \frac{1}{\omega - \omega_0 + i\alpha\omega} \right) \left( 1 + \frac{\phi_1}{\phi_0} \frac{i\omega\tau}{1 - i\omega\tau} \right). \quad (6.7)$$

Fits to the data using this model in the time domain are shown in the left panel of figure 6.4. The green line represents a response calculated using the LLG equation with a step-function change in anisotropy. Including the overshooting anisotropy dynamics has clearly improved the fit to the data. The blue line represents the difference between the data and the fit. With the exception of this short pulse near  $t=0$ , the response is now well described by the LLG equation with an overshooting anisotropy.

In the frequency domain, the allowance of an overshoot in the anisotropy also clearly resolves the line-shape into two components, with the resonant peak and sign change at low frequency both part of the magnetic response. The Fourier transform of the fast pulse

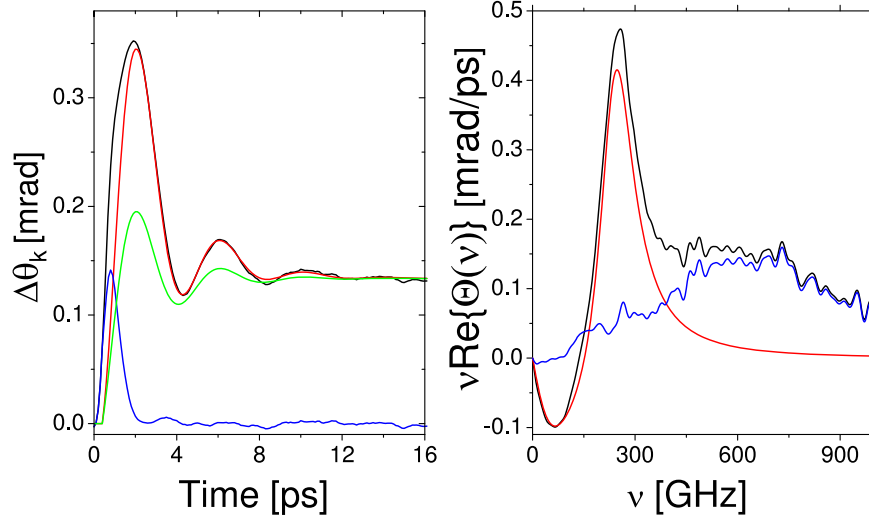


Figure 6.4: Left panel: Fit to the overshoot model in the time domain. The black line represents the data at 40K, and the red line is the fit. The blue line is the difference between the two. The green line represents a plot of the LLG equation with appropriate frequency and damping, with the amplitude set by the magnitude of the data at  $t = 20$  ps. Right panel: Fit and data in the frequency domain

in the time-domain accurately describes the high-frequency shoulder seen in the frequency domain.

### 6.3.2 Longitudinal Changes in Magnetization

The TR-MOKE signals and Fourier line-shapes contain contributions from optical effects, as well as longitudinal and transverse changes in the magnetization in response to a laser pulse. In the previous section we used a time-dependent  $h_A$  to model deviations of the data from a resonant response line-shape described by equation (6.4), while a seemingly simpler explanation for these deviations would be the addition of a longitudinal change in  $\mathbf{M}$ . However, the interpretation of the data in this description gives unphysical results for the laser induced change in the magnitude of  $\mathbf{M}$ .

The longitudinal and transverse contributions to changes in the z-component of  $\mathbf{M}$  are additive:

$$\begin{aligned} \delta M_z &= \delta(M \cos(\phi)) \\ &= (\delta M) \cos(\phi) + M(\delta \cos(\phi)). \end{aligned}$$

The longitudinal response,  $\delta M$ , accounts for ultrafast demagnetization effects as well as thermal demagnetization effects. We can model the longitudinal change with a similar function to the one we used to model the overshooting anisotropy:

$$\Delta M(t) = \Delta M_N e^{-t/\tau} + \Delta M_T. \quad (6.8)$$

Here  $\Delta M_T + \Delta M_N$ , represents the change in magnitude of  $\mathbf{M}$  due to ultrafast demagnetization, and the size of the thermal demagnetization is given by  $\Delta M_T$ . The magnetic thermalization time is represented by  $\tau$ .

The transverse response described by the LLG equation will lead to an additional thermal change in the z-projection of  $\mathbf{M}$ . The line-shape of the LLG response is governed by the precession frequency  $\omega_0$  and the damping parameter,  $\alpha$ . These parameters set the relative size of the oscillations to the final equilibrium value of  $M_z$ . The line-shape is then scaled by  $(\delta \cos(\phi))$ .

A plot of the LLG response with a frequency and damping parameter that match the data is plotted as a green line in figure 6.4. Here, the line-shape has been scaled to match the final equilibrium value of the data. For this amplitude of the LLG response, the size of the oscillations are too small to describe the data. The amplitude of the LLG response would therefore have to increase to fit the oscillations, also increasing the LLG contribution to the final equilibrium value of  $M_z$  to value higher than that of the data. To describe the data by including a longitudinal change in  $\mathbf{M}$  would then require that  $\Delta M_T < 0$ , meaning the magnitude of  $\mathbf{M}$  would have to increase in response to the thermal heating. This is an unphysical result, and therefore a model with a simple sum of transverse and longitudinal components cannot accurately describe the magnetization dynamics underlying the TRMOKE signal.

## 6.4 Parameters of the Dynamics

By including overshoot dynamics in  $\Delta h(t)$ , we are able to distinguish stimulus from response in the observed TRMOKE signals. From the LLG equation, we can extract the two parameters that describe the response: the ferromagnetic resonant frequency,  $\nu_0$ , and the damping parameter,  $\alpha$ ; and the two parameters that describe the stimulus: the relative size of the overshoot,  $\phi_1/\phi_0$  and the overshoot decay time,  $\tau_D$ .

The temperature dependence of the stimulus and response parameters is plotted in figure 6.5. The temperature dependence of the FMR frequency is very weak, with  $\Omega_{FMR}$

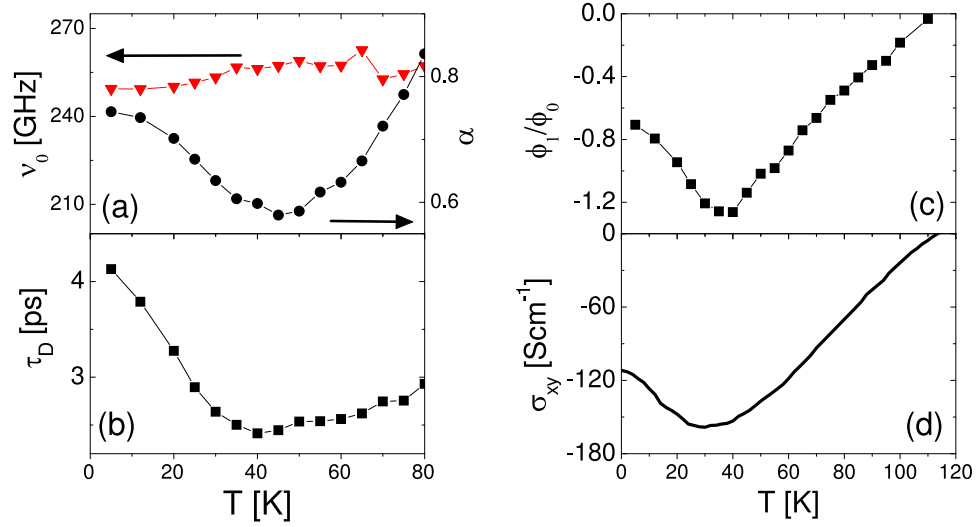


Figure 6.5: Temperature dependence of (a) FMR frequency (triangles) and damping parameter (circles), (b) overshoot decay time, (c) ratio of overshoot amplitude to step-response amplitude ( $\phi_1/\phi_0$ ), and (d)  $\sigma_{xy}$  (adapted from [64])

deviating from 250 GHz by only about 5 % over the temperature range in which oscillations are resolved. The Gilbert damping parameter  $\alpha$  is of order unity at all temperatures, a value that is approximately a factor  $10^2$  larger than found in transition metal ferromagnets. Over the same temperature range the decay of the easy axis overshoot varies from about 2 to 4 ps. The dynamical processes that characterize the response all occur in strongly overlapping time scales; the period and damping time of the FMR, and the decay time of the  $\mathbf{h}_A$  overshoot, are each in the 2-5 ps range.

#### 6.4.1 Link to the Anomalous Hall Effect

While  $\Omega_{FMR}$  is essentially independent of temperature, the parameters  $\alpha$ ,  $\phi_1/\phi_0$  and  $\tau$  exhibit structure in their temperature dependence near 40 K. This structure is reminiscent of the temperature dependence of the anomalous Hall coefficient  $\sigma_{xy}$  that has been observed in thin films of SRO [48, 27, 64]. For comparison, figure 6.5d reproduces  $\sigma_{xy}(T)$  reported in Ref. [64]. Not only does the low-temperature structure of the parameters look similar to that of  $\sigma_{xy}$ , but the temperature at which  $\sigma_{xy}$  changes signs,  $T \sim 110\text{K}$ , is the same as the temperature at which the TRMOKE signal crosses over from a decreasing decay to a rise at short times, expressed by the zero-crossing of  $\phi_1/\phi_0$ . The similarity between the temperature-dependence of AHE and parameters related to FMR suggests a possible

correlation between the two types of response functions.

Recently Nagaosa and Onoda [73] have discussed the possibility of a connection between collective spin dynamics at zero wave-vector (FMR) and the off-diagonal conductivity (AHE). At a basic level, both effects are nonzero only in the presence of both SO coupling and time-reversal breaking. A more quantitative connection is suggested by comparison of the Kubo formulas for the two corresponding functions. The off-diagonal conductivity from section 2.2.2 can be rewritten in the form [74],

$$\sigma_{xy}(\omega) = i \sum_{m,n,k} \frac{J_{mn}^x(k) J_{nm}^y(k) f_{mn}(k)}{\epsilon_{mn}(k) [\epsilon_{mn}(k) - \omega - i\gamma]}, \quad (6.9)$$

where  $J_{mn}^i(k)$  is current matrix element between quasiparticle states with band indices  $n, m$  and wave-vector  $k$ . The functions  $\epsilon_{mn}(k)$  and  $f_{mn}(k)$  are the energy and occupation difference, respectively, between such states.

FMR is related to the dynamic magnetic susceptibility, which can be calculated within the Kubo formalism by calculating the expectation value of the spin operator instead of the current operator and using a vector potential  $A$  that is appropriate for a magnetic field instead of an electric field [56]:

$$\chi_{ij}(\omega) = \sum_{m,n,k} \frac{S_{mn}^i(k) S_{nm}^j(k) f_{mn}(k)}{\epsilon_{mn}(k) - \omega - i\gamma}, \quad (6.10)$$

where  $S_{mn}^i$  is the matrix element of the spin operator. Again, the indices represent the band index, and not the spin index, since in the presence of spin-orbit coupling, spin is not a good quantum number. This denominator of this expression is only linear in the band energy difference, as opposed to quadratic for the case of the susceptibility calculation, equation (6.9). The mathematical reason for the extra factor of  $1/\epsilon_{mn}$  in the calculation of  $\sigma_{xy}$  is the inclusion of an extra factor of the vector potential in the current operator for the calculation of  $\langle J \rangle$  that isn't present in the calculation of  $\langle S \rangle$  [61].

In general,  $\sigma_{xy}(\omega)$  and  $\chi_{xy}(\omega)$  are unrelated, as they involve current and spin matrix elements respectively. However, it has been proposed that in several ferromagnets, including SRO, the  $k$ -space sums in equations (6.9) and (6.10) are dominated by a small number of band-crossings near the Fermi surface [27, 95]. If the matrix elements  $S_{mn}^i$  and  $J_{mn}^i$  vary sufficiently smoothly with  $k$ , then  $\sigma_{xy}(\omega)$  and  $\chi_{ij}(\omega)$  may both show features determined by the position of the chemical potential relative to the energy at which the bands cross.

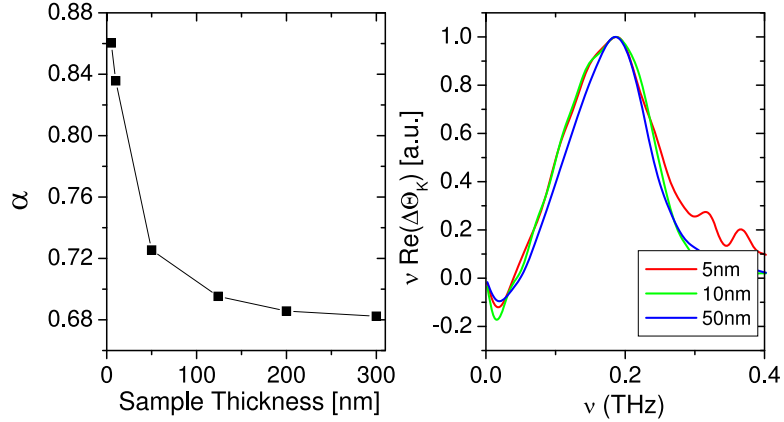


Figure 6.6: Left: Damping parameter as a function of sample thickness. Right: Fourier transforms of 5, 10, and 50 nm samples.

Furthermore, as shown in equation (6.4), the Gilbert damping is related to the zero-frequency limit of  $\chi_{ij}(\omega)$ :

$$\alpha = \frac{\Omega_{FMR}}{\chi_{ij}(0)} \frac{\partial}{\partial \omega} \lim_{\omega \rightarrow 0} \text{Im} \chi_{ij}(\omega). \quad (6.11)$$

With the anomalous hall conductivity equal to  $\sigma_{xy}(\omega = 0)$ , the band-crossing picture suggests a possible correlation between  $\alpha(T)$  and  $\sigma_{xy}(T)$ .

## 6.5 Magnetic Dynamics and Sample Thickness

The magnetization dynamics of samples with different film thicknesses indicate an increase in damping for thinner samples. Figure 6.6 shows the FT line-shapes for the thin samples ( $L < 50$  nm), and the damping parameter for all thicknesses is plotted in right right panel of the figure.

While there is some inconsistency in the properties of samples grown in different batches, the trends seen in this data do not seem to correspond with the time of growth. The 50 nm and 200 nm were grown first, followed by the 10 nm and 124 nm samples. All of these were grown by pulsed laser deposition. The 5 nm was grown by molecular beam epitaxy. Additionally, shifts in the center frequency can occur if the samples are differently positioned relative to the permanent magnet. Again, this shift in damping parameter is uncorrelated with sample position.

The shift in damping is consistent with a non-uniformly strained sample. As the

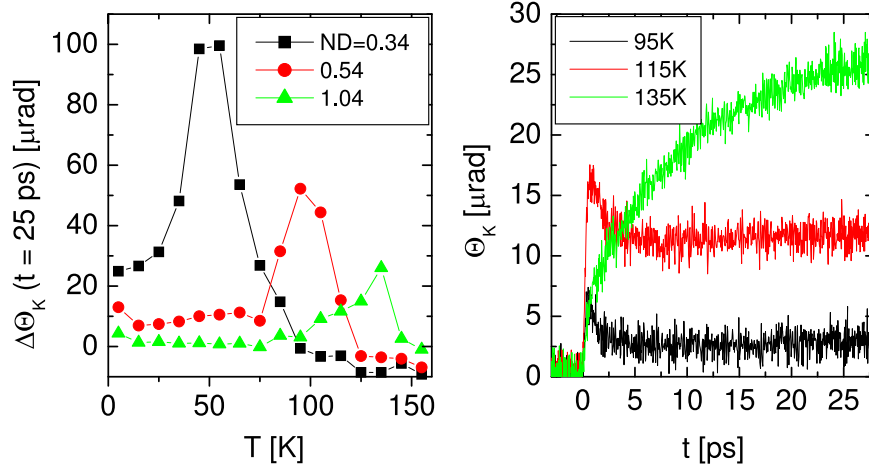


Figure 6.7: Left: TR-MOKE signal at  $t = 25$  ps on SRO single crystal for different pump attenuations. Right: Representative TR-MOKE time-traces recorder with  $ND = 1.04$ .

sample gets thinner, the TR-MOKE measurement probes the magnetization closer to the SRO/STO interface, and therefore probes more highly-strained SRO. This increase strain near creates slight changes in damping in the SRO layers within some proximity to the interface. The data suggests that the SRO film is relaxed around 125 nm.

The FT line-shapes show no evidence of standing spin-waves at any thickness. Standing spin-waves require a non-uniform excitation of the sample, and the data indicates that through relatively fast thermal diffusion, the sample is excited roughly uniformly throughout the depth of the film.

## 6.6 Magnetic Dynamics of a Single Crystal

In addition to thin film SRO on STO substrates, we studied an SRO single crystal grown by a flux-growth method. The crystal was approximately 1 mm square, with multiple flat, reflective facets, and was mounted with grease to the sample holder. A plot of the long-lived Kerr signal for different pump pulse attenuations is shown in the left panel of figure 6.7 (intensity =  $I_0 \times 10^{-ND}$ ), with representative high-temperature TR-MOKE data shown in the right panel. At low intensity, the long-lived signal shows the same temperature dependence near  $T_C$  as seen in thin films. At higher pump intensities, the peak that we associate with the magnetic transition shifts down to  $T \sim 50$  K. At low temperatures, the size of the Kerr signal does not show the strong temperature dependence seen in the thin

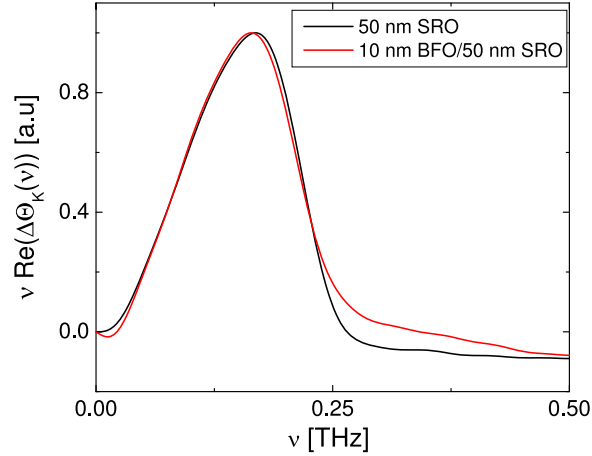


Figure 6.8: FT line shapes for a 50 nm SRO film (black), and a 50 nm SRO film with a 10 nm BFO overlayer (red).

films, and no oscillations are observed on the TR-MOKE signal. The large shift in the effect at  $T_C$  with the increase in pump intensity indicates a large amount of laser-heating, either due to the large size and low thermal conductivity of the crystal, or poor thermal contact between the crystal and the sample mount.

## 6.7 SRO/Oxide Bilayers

There is interest in SRO from a materials engineering view-point due to the close lattice-matching between SRO and other oxides. This makes it a strong candidate for the study of interfacial magnetic interaction between oxide layers. To this end, we've studied magnetization dynamics on antiferromagnetic  $\text{BiFeO}_3$ /SRO bilayers.

$\text{BiFeO}_3$  (BFO) has attracted attention as a room-temperature multiferroic, which is antiferromagnetic with a Neél temperature of 643 K and ferroelectric with a transition temperature of 1103 K, with a possibility of coupling between the antiferromagnetism and electric polarization [81, 94]. The metallic SRO layer allows for compensation of the BFO ferroelectricity, reducing the number of possible ferroelectric domains - the dipole aligns itself with the positive end oriented toward the SRO.

The BFO layer has either four or two ferroelectric domains, depending on the growth. The sample-plane projections of the ferroelectric vectors in these domains are along the  $45^\circ$  directions relative to the sides of the 5 mm by 5mm square sample, and we measure the BFO films to be birefringent along these  $45^\circ$  axes. When MOKE data is taken

with the light polarization parallel with the side of the sample ( $45^\circ$  to the birefringence axes), we see the signal shift from polarization rotation to a change in ellipticity. This shift in the phase of the signal depends on the BFO layer thickness. To reduce the effects of the birefringence, MOKE data is taken with laser polarization at  $45^\circ$  relative to the sample, along one of the birefringence axes.

The antiferromagnetic ordering direction is thought to lie in the plane perpendicular to the ferroelectric vector, with possible canting of the antiferromagnetism creating a small magnetic moment due to a Dzyaloshinskii-Moriya interaction [22]. In principle the presence of two ferroelectric domains could cause an ordering of the antiferromagnetic along the line of intersection between the two perpendicular planes, creating a favored magnetic direction in the BFO.

Unfortunately, no evidence of coupling has yet to be seen in the SRO magnetization dynamics due the BFO magnetization. Figure 6.7 shows the FT line-shapes for an SRO sample and for a BFO/SRO bilayer sample. The data exhibit a slight difference in the high-frequency response but minimal difference in line-shape associated with the magnetic precession.

More promising results have been seen in continuing work being carried out by Colleen Kantner in the study of superconducting  $\text{YBa}_2\text{C}_3\text{O}_7$ /SRO bilayers. In samples with  $\text{YBa}_2\text{C}_3\text{O}_7$  (YBCO) layers in which the oxygen content has been altered such that the film is non-superconducting at all temperatures, no change in dynamics is seen. Bilayer systems with a superconducting YBCO film show a reduction in the size of the quasi-equilibrium change in the magnetization when the sample is cooled through the YBCO superconducting transition temperature, indicating a change in the SRO magnetization due to the superconducting state.

## Chapter 7

# Summary

This thesis has focused on the ultrafast optical measurement and analysis of magnetization dynamics in SRO thin films. In spite of the large amount of research that has been done on this material, our results are the first characterization of the ferromagnetic resonance, as ultrafast optics allow us to measure the magnetic resonance at a frequency beyond what can be measured from a standard FMR experiment.

The analysis of the TR-MOKE signal can be divided cleanly between two different time regimes. At times longer than 20 ps, the precessional dynamics have damped out, and the different thermal baths can be regarded as being at thermal equilibrium. For time-scales shorter than 20 ps, the signal is dominated by the motion of the magnetization vector in response to the laser-induced reorientation of the easy axis.

If the long-time signal represents a thermal equilibrium state in the sample, the energy deposited by the pump pulse is converted into thermal energy, giving a well-defined relationship between the pump energy and rise in temperature. We explore this relationship by varying the pump power and tuning the substrate temperature, and we find the relationship to be consistent with an interpretation of thermal excitation. Analysis of the induced change in temperature provides evidence of a magnon-dominated thermal energy at higher temperatures than in elemental ferromagnets. This result suggests relatively weak spin-exchange coupling and is consistent with the low magnetic transition temperature measured in SRO.

The transport of the deposited laser energy out of the film is limited by the film/substrate interface. The electrons and magnons are confined to the film, and only the phonons can carry thermal energy across the interface. Phonon reflection and scattering are commonly proposed descriptions for thermal boundary resistance, however the

temperature dependence of the thermal decay times suggest that this description is not accurate for SRO/STO films. For a phonon mismatch boundary resistance the decay time should have a strong T-dependence due to differences in the T-dependence of thermally occupied states for magnons, which dominate the sample thermal energy, and phonons, which transfer the energy to the substrate.

Additional boundary resistance exists due to non-equilibrium between the phonons and electron/magnon fluid at the interface, that occurs as a result of different boundary conditions for the fluids at the interface. This effective resistance is distinguishable from a phonon mismatch resistance only by the finite region over which the phonon temperature drop occurs, and has not been observed experimentally. The weak T-dependence of the thermal decay times is consistent with a model in which the effective resistance from phonon/electron non-equilibrium is limiting heat transfer into the substrate.

On shorter time-scales, the magnetization dynamics are well described by the LLG equation, combined with a time-dependent change in the anisotropy direction after laser excitation. The shape of the TR-MOKE signal is not consistent with a simple LLG response or an LLG response combined with a longitudinal change in the magnetization. From modeling of the magnetic dynamics, we are able to extract the parameters that describe both the precession of the magnetization as well as the easy axis motion. The size of the easy-axis overshoot shows a similar temperature dependence to that observed in the anomalous Hall conductivity. We propose that this similarity is a result of near-degeneracy points in the band structure that dominate both the anomalous Hall conductivity and the magnetic susceptibility.

# Bibliography

- [1] Y Acremann, C H Back, M Buess, O Portmann, A Vaterlaus, D Pescia, and H Melchior. Imaging precessional motion of the magnetization vector. *Science*, 290(5491):492–495, 2000.
- [2] P.B. Allen, H. Berger, O. Chauvet, L. Forro, T. Jarlborg, A. Junod, B. Revaz, and G. Santi. Transport properties, thermodynamic properties, and electronic structure of SrRuO<sub>3</sub>. *Physical Review B*, 53(8):4939–4944, 1996.
- [3] Neil W. Ashcroft and N. David Mermin. *Solid State Physics*. Harcourt College Publishers, Fort Worth, Texas, 1976.
- [4] W. Baltensperger and J.S. Helman. A model that gives rise to effective dry friction in micromagnetics. *Journal of Applied Physics*, 73(10):6516–6518, 1993.
- [5] E. Beaurepaire, J.-C. Merle, A. Daunois, and J.-Y. Bigot. Ultrafast spin dynamics in ferromagnetic nickel. *Physical Review Letters*, 76(22):4250–4253, 1996.
- [6] M.N. Berberan-Santos, E.N. Bodunov, and B. Valeur. Mathematical functions for the analysis of luminescence decays with underlying distributions 1. kohlrausch decay function (stretched exponential). *Chemical Physics*, 315:171–182, 2005.
- [7] L. Berger. Side-jump mechanism for the hall effect in ferromagnets. *Physical Review B*, 2(11):4559–4566, 1970.
- [8] G. Bergmann. Analysis of the anomalous hall effect in a double layer of a ferromagnetic and a normal metal. *European Physical Journal B*, 54:19–25, 2006.
- [9] J.A.C. Bland and B. Heinrich. *Ultrathin Magnetic Structures I*. Springer-Verlag, Berlin, Germany, 1994.
- [10] W. F. Brown. *Micromagnetics*. Krieger, 1963.

- [11] P. Bruno, Y. Suzuki, and C. Chappert. Magneto-optical kerr effect in a paramagnetic overlayer on a ferromagnetic substrate: A spin-polarized quantum size effect. *Physical Review B*, 53(14):9214–9220, 1996.
- [12] David G. Cahill, Wayne K. Ford, Kenneth E. Goodson, Gerald D. Mahan, Arun Majumdar, Humphrey J. Maris, Roberto Merlin, and Simon R. Phillpot. Nanoscale thermal transport. *Applied Physics Reviews*, 93(2):793–818, 2003.
- [13] John Rozier Cannon and Felix E. Browder. *The One-Dimensional Heat Equation*. Cambridge University Press, New York, New York, 1984.
- [14] G. Cao, O. Korneta, S. Chikara, L.E. DeLong, and P. Scholttmann. Non-fermi-liquid behavior in single-crystal  $\text{CaRuO}_3$ : Comparison to ferromagnetic  $\text{SrRuO}_3$ . *Solid State Communications*, 148:305–309, 2008.
- [15] G Cao, S McCall, M Shepard, J E Crow, and R P Guertin. Thermal, magnetic, and transport properties of single-crystal  $\text{Sr}_{1-x}\text{Ca}_x\text{RuO}_3$  ( $0 \leq x \leq 1.0$ ). *Phys. Rev. B*, 56(1):321–329, 1997.
- [16] G. Cao, W.H. Song, Y.P. Sun, X.N. Lin, and J.E. Crow. Violation of the mott-ioffe-regel limit: High-temperature resistivity of itinerant magnets  $\text{Sr}_{n+1}\text{Ru}_n\text{O}_{3n+1}$  and  $\text{CaRuO}_3$ . *condmat*, 1998. <http://arxiv.org/ftp/cond-mat/papers/0311/0311142.pdf>.
- [17] John Cardy. *Scaling and Renormalization in Statistical Physics*. Cambridge University Press, New York, New York, 1996.
- [18] Sushin Chikazumi. *Physics of Magnetism*. Krieger Publishing Company, Malabar, Florida, 1978.
- [19] M. Cinchetti, M. Sánchez Albaneda, D. Hoffmann, T. Roth, J.P. Wustenberg, M. Krau, O. Andreyev, H.C. Schneider, M. Bauer, and M. Aeschlimann. Spin-flip processes and ultrafast magnetization dynamics in co: Unifying the microscopic and macroscopic view of femtosecond magnetism. *Physical Review Letters*, 97:177201, 2006.
- [20] Bruce M. Clemens, Gary L. Eesley, and Carolyn A. Paddock. Time-resolved thermal transport in compositionally modulated metal films. *Physical Review B*, 37(3):1085–1097, 1988.

- [21] Mary F. Doerner and William D. Nix. Stresses and deformation processes in thin films on substrates. *Critical Reviews in Solid State and Materials Sciences*, 14(3):225–268, 1988.
- [22] C. Ederer and N.A. Spaldin. Weak ferromagnetism and magnetoelectric coupling in bismuth ferrite. *Physical Review B*, 71(6):060401, 2005.
- [23] V.J. Emery and S.A. Kivelson. Superconductivity in bad metals. *Physical Review Letters*, 74(16):3253–3256, 1995.
- [24] J. Fabian and S. Das Sarma. Spin relaxation of conduction electrons in polyvalent metals: Theory and a realistic calculation. *Physical Review Letters*, 81(25):5624–5627, 1998.
- [25] J. Fabian and S. Das Sarma. Phonon-induced spin relaxation of conduction electrons in aluminum. *Physical Review Letters*, 83(6):1211–1214, 1999.
- [26] L.M. Falicov, Daniel T. Pierce, S.D. Bader, R. Gronsky, Kristl B. Hathaway, Herbert J. Hopster, David N. Lambeth, S.S.P. Parkin, Gary Prinz, Myron Salamon, Ivan K. Schuller, and R.H. Vitora. Surface, interface, and thin-film magnetism. *Journal of Materials Research*, 5(6):1299–1340, 1990.
- [27] Z. Fang, N. Nagaosa, K.S. Takahashi, A. Asamitsu, R. Mathieu, T. Ogasawara, H. Yamada, M. Kawasaki, Y. Tokura, and K. Terakura. The anomalous hall effect and magnetic monopoles in momentum space. *Science*, 302(5642):92–95, 2003.
- [28] K. Fujioka, J. Okamoto, T. Mizokawa, A. Fujimori, I. Hase, M. Abbate, H.J. Lin, C.T. Chen, Y. Takeda, and M. Takano. Electronic structure of SrRuO<sub>3</sub>. *Physical Review B*, 56(11):6380–6383, 1997.
- [29] Q. Gan, R.A. Rao, C.B. Eom, J.L. Garrett, and Mark Lee. Direct measurement of strain effects on magnetic and electrical properties of epitaxial SrRuO<sub>3</sub> thin films. *Applied Physics Letters*, 72(8):978–980, 1997.
- [30] Stephen Gasiorowicz. *Quantum Physics*. John Wiley & Sons, New York, New York, 1996.
- [31] Paul Gordon. Nonsymmetric difference equations. *Journal of the Society for Industrial and Applied Mathematics*, 13(3):667–673, 1965.

- [32] Bretislav Heinrich. In J.A.C. Bland and B. Heinrich, editors, *Ultrathin Magnetic Structures II*. Springer-Verlag, Berlin, Germany, 1994.
- [33] B. Heinrich. In J.A.C. Bland and B. Heinrich, editors, *Ultrathin Magnetic Structures III*. Springer-Verlag, Berlin, Germany, 2005.
- [34] W K Hiebert, A Stankiewicz, and M R Freeman. Direct observation of magnetic relaxation in a small permalloy disk by time-resolved scanning kerr microscopy. *Phys. Rev. Lett.*, 79(6):1134–1137, 1997.
- [35] Burkard Hillebrands. In M. Cardona and G. G unterhodt, editors, *Light Scattering in Solids VII*. Springer-Verlag, Berlin, Germany, 2000.
- [36] J.C. Jiang, W. Tian, X.Q. Pan, Q. Gan, and C.B. Eom. Domain structure of epitaxial SrRuO<sub>3</sub> thin films on miscut (001) SrTiO<sub>3</sub> substrates. *Applied Physics Letters*, 72(23):2963–2965, 1998.
- [37] M.T. Johnson, P.J.H. Bloemen, F.J.A. den Broeder, and J.J. de Vries. Magnetic anisotropy in metallic multilayers. *Reports on Progress in Physics*, 59:1409–1458, 1996.
- [38] Y. Sungtaek Ju. Impact of nonequilibrium between electrons and phonons on heat transfer in metallic nanoparticles suspended in dielectric media. *Journal of Heat Transfer*, 127:1400–1402, 2005.
- [39] Y. Sungtaek Ju, Ming-Tsung Hung, and Takane Usui. Nanoscale heat conduction across metal-dielectric interfaces. *Journal of Heat Transfer*, 128:919–925, 2006.
- [40] V. Kamberský. On the Landau-Lifshitz relaxation in ferromagnetic metals. *Canadian Journal of Physics*, 48:2906–2911, 1970.
- [41] D. Kirillov, Y. Suzuki, L. Antognazza, K. Char, I. Bozovic, and T.H. Geballe. Phonon anomalies at the magnetic phase transition in SrRuO<sub>3</sub>. *Journal of the Society for Industrial and Applied Mathematics*, 51(18):12825–12828, 1995.
- [42] T. Kise, T. Ogasawara, M. Ashida, Y. Tamioka, Y. Tokura, and M. Kuwata-Gonokami. Ultrafast spin dynamics and critical behavior in half-metallic ferromagnet: Sr<sub>2</sub>FeMoO<sub>6</sub>. *Physical Review Letters*, 85(9):1986–1989, 2000.

- [43] T. Kiyama, K. Yoshimura, K. Kosuge, Y. Ikeda, and Y. Bando. Invar effect of SrRuO<sub>3</sub>: Itinerant electron magnetism of Ru 4d electrons. *Physical Review B*, 54(2):R756–R759, 1996.
- [44] L Klein, J S Dodge, C H Ahn, J W Reiner, L Mieville, T H Geballe, M R Beasley, and A Kapitulnik. Transport and magnetization in the badly metallic itinerant ferromagnet SrRuO<sub>3</sub>. *J. Phys. Cond.-Matter*, 8(48):10111–10126, 1996.
- [45] L. Klein, J.S. Dodge, C.H. Ahn, G.J. Snyder, T.H. Geballe, M.R. Beasley, and A. Kapitulnik. Anomalous spin scattering effects in the badly metallic itinerant ferromagnet SrRuO<sub>3</sub>. *Physical Review Letters*, 77(13):2774–2777, 1996.
- [46] L. Klein, J.S. Dodge, T. H. Geballe, A. Kapitulnik, A.F. Marshall, L. Antognazza, and K. Char. Perpendicular magnetic anisotropy and strong magneto-optic properties of SrRuO<sub>3</sub> epitaxial films. *Applied Physics Letters*, 66(18):2427–2429, 1995.
- [47] L. Klein, J.S. Dodge, T.H. Geballe, A. Kapitulnik, A.F. Marshall, L. Antognazza, and K. Char. Perpendicular magnetic anisotropy and strong magneto-optic properties of SrRuO<sub>3</sub> epitaxial films. *Applied Physics Letters*, 66(18):2427–2429, 1995.
- [48] L Klein, J R Reiner, T H Geballe, M R Beasley, and A Kapitulnik. Extraordinary hall effect in SrRuO<sub>3</sub>. *Phys. Rev. B*, 61(12):R7842–R7845, 2000.
- [49] T. Kobayashi, R. Barker, and A. Yelon. Ferromagnetoelastic resonance in thin films. II. application to nickel. *Physical Review B*, 7(7):3286–3297, 1973.
- [50] B. Koopmans, Ruigrok J.J.M., F. Dalla Longa, and W.J.M. de Jonge. Unifying ultrafast magnetization dynamics. *Physical Review Letters*, 95:267207, 2005.
- [51] B. Koopmans, M. van Kampen, J. T. Kohlhepp, and W. J. M. de Jonge. Ultrafast magneto-optics in nickel: Magnetism or optics? *Phys. Rev. Lett.*, 85(4):844, 2000.
- [52] Bert Koopmans. In Burkard Hillebrands and Kamel Ounadjela, editors, *Spin Dynamics in Confined Magnetic Structures II*. Springer-Verlag, Berlin, Germany, 2003.
- [53] V. Korenman and R.E. Prange. Damping of spin waves in magnetic metals. *Physical Review B*, 6(7):2769–2777, 1972.
- [54] P. Kostic, Y. Okada, N.C. Collins, Z. Schlesinger, J.W. Reiner, L. Klein, A. Kapitulnik, T.H. Geballe, and M.R. Beasley. Non-fermi liquid behavior of SrRuO<sub>3</sub>: Evidence from infrared conductivity. *Physical Review Letters*, 81(12):2498–2501, 1998.

- [55] M.S. Laad and E. Muller-Hartmann. Origin of the non-fermi liquid behavior of SrRuO<sub>3</sub>. *Physical Review Letters*, 87(24):246402, 2001.
- [56] Laurent-Patrick Lévy. *Magnetism and Superconductivity*. Springer-Verlag, Berlin, Germany, 2000.
- [57] J. Lindner, K. Lenz, E. Kosubek, K. Baberschke, D. Spoddig, R. Meckenstock, J. Pelzl, Z. Frait, and M.L. Mills. Non-gilbert-type damping of the magnetic relaxation in ultrathin ferromagnets: Importance of magnon-magnon scattering. *Physical Review B*, 68:060102, 2003.
- [58] J.M. Longo, P.M. Raccah, and J.B. Goodenough. Magnetic properties of SrRuO<sub>3</sub> and CaRuO<sub>3</sub>. *Journal of Applied Physics*, 39(2):2963–2965, 1968.
- [59] J. M. Luttinger and R. Karplus. Hall effect in ferromagnets. *Physical Review*, 94(3):782, 1954.
- [60] Arun Majumdar and Pramod Reddy. Role of electronphonon coupling in thermal conductance of metal/nonmetal interfaces. *Applied Physics Letters*, 84(23):4768–4770, 2004.
- [61] Michael P. Marder. *Condensed Matter Physics*. John Wiley & Sons, New York, New York, 2000.
- [62] A F Marshall, L Klein, J S Dodge, C H Ahn, J W Reiner, L Mieville, L Antagonazza, A Kapitulnik, T H Geballe, and M R Beasley. Lorentz transmission electron microscope study of ferromagnetic domain walls in SrRuO<sub>3</sub>: Statics, dynamics, and crystal structure correlation. *J. Appl. Phys.*, 85(8, Part 1):4131–4140, 1999.
- [63] Imada Masatoshi, Atsushi Fujimori, and Yoshinori Tokura. Metal-insulator transitions. *Reviews of Modern Physics*, 70(4):1039–1263, 1998.
- [64] R. Mathieu, A. Asamitsu, H. Yamada, K. S. Takahashi, M. Kawasaki, Z. Fang, N. Nagao, and Y. Tokura. Scaling of the anomalous hall effect in Sr<sub>1-x</sub>Ca<sub>x</sub>RuO<sub>3</sub>. *Phys. Rev. Lett.*, 93(1):016602, 2004.
- [65] D.L. Mills and S.M. Rezende. In B. Hillibrands and K. Ounadjela, editors, *Spin Dynamics in Confined Magnetic Structures II*. Springer-Verlag, Berlin, Germany, 2003.

- [66] J. Miltat, G. Albuquerque, and A. Thiaville. In Burkard Hillebrands and Kamel Ounadjela, editors, *Spin Dynamics in Confined Magnetic Structures I*. Springer-Verlag, Berlin, Germany, 2002.
- [67] P. Monod and F. Beuneu. Conduction-electron spin flip by phonons in metals: Analysis of experimental data. *Physical Review B*, 19(2):911–916, 1979.
- [68] Naoto Nagaosa. Anomalous hall effect - a new perspective. *Journal of the Physical Society of Japan*, 75(4):042001, 2006.
- [69] Theodore C. Oakley. Magneto-optical kerr effect. Technical report, Hinds Instruments, INC, Hillsboro, Oregon, 2005.
- [70] T Ogasawara, K Ohgushi, Y Tomioka, K S Takahashi, H Okamoto, M Kawasaki, and Y Tokura. General features of photoinduced spin dynamics in ferromagnetic and ferrimagnetic compounds. *Physical Review Letters*, 94(8):087202, 2005.
- [71] A. Okazaki and M. Kawaminami. Lattice constant of strontium titanate at low temperatures. *Materials Research Bulletin*, 8:545, 1973.
- [72] N.P. Ong and Wei-Li Lee. Geometry and the anomalous hall effect in ferromagnets. *condmat*, 2005. <http://arxiv.org/abs/cond-mat/0508236v1>.
- [73] M. Onoda, A.S. Mishchenko, and N. Nagaosa. Left-handed ferromagnet. *arXiv:cond-mat/0702379v1*, 2007.
- [74] M Onoda and N Nagaosa. Topological nature of anomalous hall effect in ferromagnets. *J. Phys. Soc. Jap.*, 71(1):19–22, 2002.
- [75] Shigeki Onoda, Naoyuki Sugimoto, and Naoto Nagaosa. Intrinsic versus extrinsic anomalous hall effect in ferromagnets. *Physical Review Letters*, 97:126602, 2006.
- [76] L. Pálová, P. Chandra, and K.M. Rabe. Modelling the dependence of properties of ferroelectric thin film on thickness. *Physical Review B*, 76:014112, 2007.
- [77] J.C. Phillips. Stretched exponential relaxation in molecular and electronic glasses. *Reports on Progress in Physics*, 59:1133–1207, 1996.
- [78] M. Pickel, A. B. Schmidt, F. Giesen, J. Braun, J. Minár, H. Ebert, M. Donath, and M. Weinelt. Spin-orbit hybridization points in the face-centered-cubic cobalt band structure. *Physical Review Letters*, 101:066402, 2006.

- [79] Stefania Pizzini, Jan Vogel, Marlio Bonfim, and Alain Fontaine. In Burkard Hillebrands and Kamel Ounadjela, editors, *Spin Dynamics in Confined Magnetic Structures II*. Springer-Verlag, Berlin, Germany, 2003.
- [80] K. Presz and R.W. Munn. Densities of states and anisotropy in tight-binding models. *Journal of Physics C: Solid State Physics*, 19:2499–2507, 1986.
- [81] R. Ramesh and Nicola A. Spaldin. Multiferroics: progress and prospects in thin films. *Nature Materials*, 6:1719–1722, 2007.
- [82] A. Savitzky and M.J.E. Golay. Smoothing and differentiation of data by simplified least squares procedures. *Analytical Chemistry*, 36:1627–1639, 1964.
- [83] M. Shimizu. Itinerant electron magnetism. *Reports on Progress in Physics*, 44:330–409, 1981.
- [84] K. Shinagawa. In S. Sugano and K. Norimichi, editors, *Magneto-Optics*, volume 128 of *Solid State Sciences*. Springer-Verlag, Berlin, Germany, 2000.
- [85] N.A. Sinitsyn. Semiclassical theories of the anomalous hall effect. *condmat*, 2007. <http://arxiv.org/abs/0712.0183v2>.
- [86] Ralph Skomski. *Simple Models of Magnetism*. Oxford University Press, Oxford, 2008.
- [87] J. Smit. Magnetoresistance of ferromagnetic metals and alloys at low temperatures. *Physica*, 16(6):612–627, 1951.
- [88] Joachim Stöhr and Hans Christoph Siegmann. *Magnetism: From Fundamentals to Nanoscale Dynamics*. Springer-Verlag, Berlin, Germany, 2006.
- [89] C.-K. Sun, F. Vallée, L. Acioli, E.P. Ippen, and J.G. Fujimoto. Femtosecond investigation of electron thermalization in gold. *Physical Review B*, 48(6):12365–12368, 1993.
- [90] Masuo Suzuki, Kunihiko Kaneko, and Shinji Takesue. Critical slowing down in stochastic processes. *Progress of Theoretical Physics*, 67(6):1756–1775, 1982.
- [91] E.T. Swartz and R.O. Pohl. Thermal boundary resistance. *Reviews of Modern Physics*, 61(3):605–668, 1989.

- [92] Guray Tas and Humphrey J. Maris. Electron diffusion in metals studied by picosecond ultrasonics. *Physical Review B*, 49(21):15046–15054, 1994.
- [93] M van Kampen, C Jozsa, J T Kohlhepp, P LeClair, L Lagae, W J M de Jonge, and B Koopmans. All-optical probe of coherent spin waves. *Phys. Rev. Lett.*, 88(22):227201, 2002.
- [94] J. Wang, J.B. Neaton, H. Zheng, V. Nagarajan, S.B. Ogale, B. Liu, D. Viehland, V. Vaithyanathan, D.G. Schlom, U.V. Waghmare, N.A. Spaldin, K.M. Rabe, M. Wuttig, and R. Ramesh. Epitaxial BiFeO<sub>3</sub> multiferroic thin film heterostructures. *Science*, 299:22–29, 2003.
- [95] X. Wang, J. R. Yates, I. Souza, and D. Vanderbilt. Ab initio calculation of the anomalous hall conductivity by wannier interpolation. *Phys. Rev. B.*, 74:195118, 2006.
- [96] Shinsuke Yamanaka, Takuji Maekawa, Hiroaki Muta, Tetsushi Matsuda, Shin-ichi Kobayashi, and Ken Kurosaki. Thermophysical properties of SrHfO<sub>3</sub> and SrRuO<sub>3</sub>. *Journal of Solid State Chemistry*, 177:3484–3489, 2004.
- [97] Chun Yeol You and Sung-Chul Shin. Derivation of simplified analytic formulae for magneto-optical kerr effects. *Applied Physics Letters*, 69(9):1315–1317, 1996.
- [98] J. Zak, E.R. Moog, C. Liu, and S.D. Bader. Universal approach to magneto-optics. *Journal of Magnetism and Magnetic Materials*, 89:107–123, 1990.
- [99] A.T. Zayak, X. X. Huang, J.B. Neaton, and Karin M. Rabe. Structural, electronic, and magnetic properties of SrRuO<sub>3</sub> under epitaxial strain. *Physical Review B*, 74:094104, 2006.
- [100] G.P. Zhang and W. Hubner. Laser-induced ultrafast demagnetization in ferromagnetic metals. *Physical Review Letters*, 85(14):3025–3028, 2000.
- [101] Guoping Zhang, Wolfgang Hubner, Eric Beaurepaire, and Jean-Yves Bigot. In Burkard Hillebrands and Kamel Ounadjela, editors, *Spin Dynamics in Confined Magnetic Structures I*. Springer-Verlag, Berlin, Germany, 2002.